iScience

CellPress

Article

Modification of TiO_2 Nanoparticles with Organodiboron Molecules Inducing Stable Surface Ti^{3+} Complex

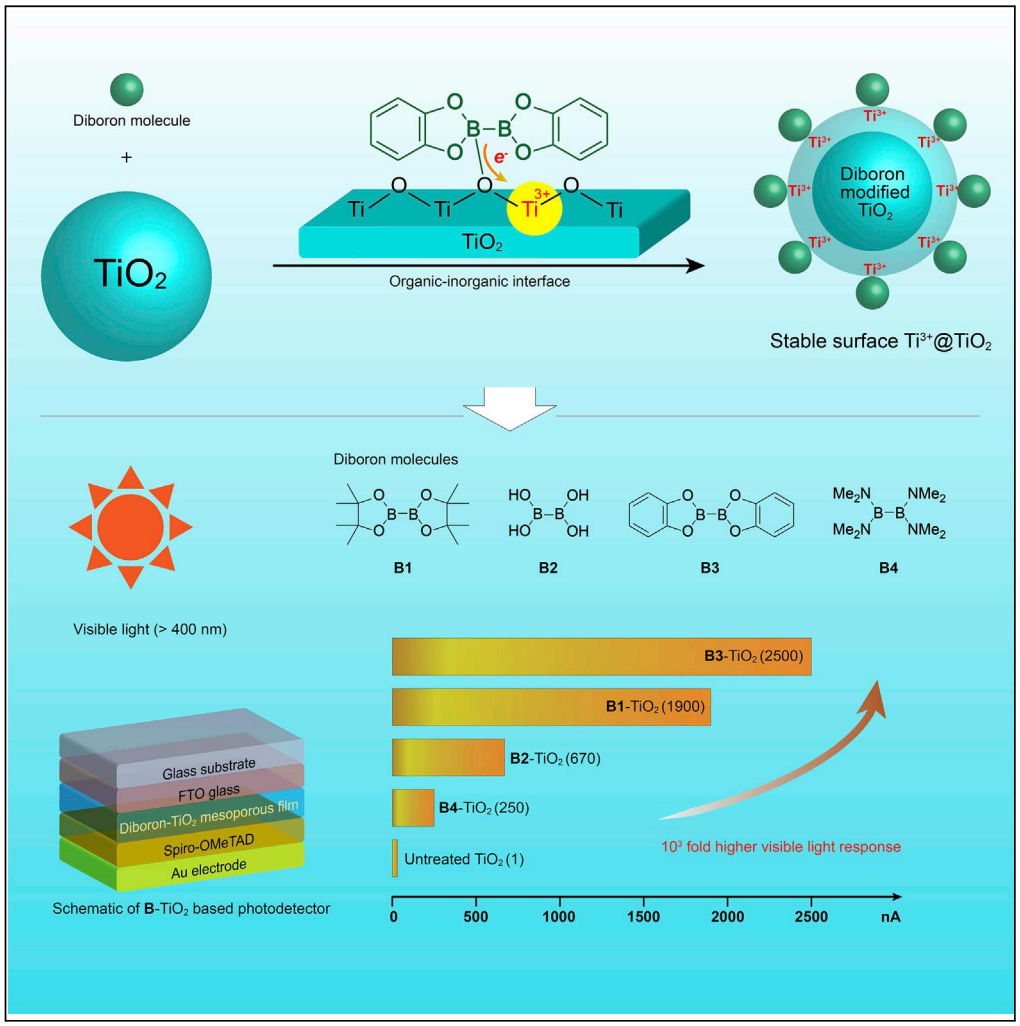

Yang Cao, Peng Zhou, Yongguang Tu, ..., Shaojun Guo, Fanyang Mo, Wanhong Ma

fmo@pku.edu.cn

HIGHLIGHTS

Organodiborons are used to reshape the surface electronic state of semiconductor oxides

Diboron adsorption leads to spontaneous charge transfer and reduced surface metal ions

Photodetector based on diboron material affords 10^3 fold higher visible light response

Cao et al., iScience 20, 195–204
October 25, 2019
https://doi.org/10.1016/j.isci.2019.09.024

iScience

CellPress

Article

Modification of TiO_2 Nanoparticles with Organodiboron Molecules Inducing Stable Surface Ti^{3+} Complex

Yang Cao,[1,12] Peng Zhou,[2,12] Yongguang Tu,[3,4,12] Zheng Liu,[5] Bo-Wei Dong,[5] Aryan Azad,[1] Dongge Ma,[6] Dong Wang,[1] Xu Zhang,[7] Yang Yang,[8] Shang-Da Jiang,[5] Rui Zhu,[3,9] Shaojun Guo,[1,2] Fanyang Mo,[1,10,13,*] and Wanhong Ma[11]

SUMMARY

As one of the most promising semiconductor oxide materials, titanium dioxide (TiO_2) absorbs UV light but not visible light. To address this limitation, the introduction of Ti^{3+} defects represents a common strategy to render TiO_2 visible-light responsive. Unfortunately, current hurdles in Ti^{3+} generation technologies impeded the widespread application of Ti^{3+} modified materials. Herein, we demonstrate a simple and mechanistically distinct approach to generating abundant surface-Ti^{3+} sites without leaving behind oxygen vacancy and sacrificing one-off electron donors. In particular, upon adsorption of organodiboron reagents onto TiO_2 nanoparticles, spontaneous electron injection from the diboron-bound O^{2-} site to adjacent Ti^{4+} site leads to an extremely stable blue surface Ti^{3+}–$O^{-\cdot}$ complex. Notably, this defect generation protocol is also applicable to other semiconductor oxides including ZnO, SnO_2, Nb_2O_5, and In_2O_3. Furthermore, the as-prepared photoelectronic device using this strategy affords 10^3-fold higher visible light response and the fabricated perovskite solar cell shows an enhanced performance.

INTRODUCTION

Owing to its abundance, nontoxicity, and stability, semiconductor oxide (TiO_2, ZnO, SnO_2, etc.) nanoparticles and films have been widely used as wide-band-gap semiconductor photocatalysts for a variety of solar-driven clean energy and environmental technologies, such as photovoltaics and photocatalytic fuel generation (Chen and Mao, 2007; Grätzel, 2001). However, pristine wide band semiconductor oxides is not an appropriate candidate for practical applications since it only adsorbs UV light. The optical response of TiO_2 nanocrystal has been tuned to visible region using band gap engineering techniques, including metallic (Dahl et al., 2014; Hoffmann et al., 1995) or nonmetallic (Asahi et al., 2001, 2014; Chen and Burda, 2008; Khan et al., 2002) impurity doping, solid solution formation (Maeda et al., 2006; Wang et al., 2008), and self-structural modification (Liu and Chen, 2014). Among various self-modification techniques, *in situ* formation of self-doped Ti^{3+} in the bulk phase through the introduction of oxygen vacancy at high temperature is an effective strategy for band gap engineering (Figure 1A) (Zuo et al., 2010). Additionally, hydrogenation of TiO_2 nanocrystals can also result in visible-light-responsible materials (Chen et al., 2011). The latest studies show that these low-energy absorption materials arouse utilities in visible light water splitting and microwave and terahertz absorption (Green et al., 2018a, 2018b, 2019a, 2019b; Guan and Chen, 2018; Tian et al., 2017). Unfortunately, harsh reaction conditions and long-time treatment have limited the practicality of these methods, especially in the context of on-site fabrication and reprocessing of light harvesting devices. Alternatively, UV irradiation of TiO_2 nanoparticles (Schrauben et al., 2012) or visible light irradiation of dye-sensitized systems can also produce visible-light-responsive blue-surface TiO_2 (Figure 1B) (Yan et al., 2017). In both cases, organic sacrificial agents are required, and these agents are irreversibly oxidized by photoinduced holes (e.g., alcohol to aldehyde and I^- to I_2). Moreover, such nascent optically active Ti^{3+} center is highly unstable toward O_2 owing to instantaneous oxidation to Ti^{4+}. To our knowledge, the formation of air-stable surface Ti^{3+} centers using these techniques has not been previously described. We surmise that this is largely due to the difficulty in stabilizing the key Ti^{3+}–O^{2-} moiety formed in these processes, as such moiety is highly reactive toward O_2 to afford Ti^{4+}–O–$O^{-\cdot}$. In light of these constraints, the ability to access air-stable surface Ti^{3+} defects within TiO_2 would represent a paradigm shift for the field of TiO_2-based oxide semiconducting materials. In this report, we show that this goal can be accomplished through the simultaneous modification of surface O^{2-} and Ti^{4+} sites in TiO_2 to afford a persistent, optically active Ti^{3+}–$O^{-\cdot}$ species.

[1]Department of Energy and Resources Engineering, College of Engineering, Peking University, Beijing 100871, China

[2]Department of Materials Science and Engineering, College of Engineering, Peking University, Beijing 100871, China

[3]State Key Laboratory for Artificial Microstructure and Mesoscopic Physics, School of Physics, Frontiers Science Center for Nano-optoelectronics & Collaborative Innovation Center of Quantum Matter, Peking University, Beijing 100871, China

[4]Shaanxi Institute of Flexible Electronics, Northwestern Polytechnical University, Xi'an, Shaanxi 710072, China

[5]Beijing National Laboratory for Molecular Sciences, College of Chemistry and Molecular Engineering, Peking University, Beijing 100871, China

[6]School of Science, Beijing Technology and Business University, Beijing 100048, China

[7]Department of Physics and Astronomy, California State University Northridge, Northridge, CA 91330, USA

[8]Division of Chemistry and Chemical Engineering, California Institute of Technology, Pasadena, CA 91125, USA

[9]Collaborative Innovation Center of Extreme Optics, Shanxi University, Taiyuan, Shanxi 030006, China

[10]Jiangsu Donghai Silicon Industry S&T Innovation Center, Donghai County, Jiangsu 222300, China

Continued

Organodiboron compounds constitute a class of stable and highly versatile reagents commonly used in organic synthesis (Neeve et al., 2016). Despite their unique reactivity, to date, the use of these diboron species in the modification of inorganic materials remains surprisingly scarce. Herein, we report a new method for the facile generation of Ti^{3+} defects on TiO_2 surface under mild conditions (<80°C) enabled by the use of diboron reagents (Figure 1C). In this process, facilitated by the intimate interaction of the diboron reagent's B center with the surface bridging O_{2c} of TiO_2, the adsorption of organodiboron reagents onto TiO_2 nanoparticles leads to spontaneous electron transfer, resulting in a stable, blue surface Ti^{3+}-TiO_2. Notably, this process does not require complicated synthetic manipulations such as anaerobic photo irradiation or high temperature calcination, which are commonly employed by previously developed techniques.

Previously developed strategies for TiO_2 surface modification have mainly focused on the modification of surface Ti sites with organic nucleophiles (e.g., phenol, alcohol, and carboxylic acids). In contrast, surface bridging oxygen (O_{2c}) sites have seldom been functionalized with electrophilic organic reagents. We posited that electrophilic organic adsorbates with an appropriate reduction potential might favorably interact with the surface O_{2c} sites. Importantly, this binding event might overcome the barrier of electron transfer from O^{2-} sites to adjacent Ti^{4+} sites and further stabilize the primary charge separation state. We were particularly interested in the use of organic diboron reagents because of their unique Lewis acidity and reducing ability (*vide supra*). Previous work in the area of synthetic organic chemistry showed that, upon binding to a Lewis basic oxygen atom, these organic diboron species can function as single electron reducing agents, thus allowing for various important transformations (Liu et al., 2019; Mo et al., 2010, 2018; Pietsch et al., 2015; Wang et al., 2016; Zhang and Jiao, 2017). Based on these reasons, we envisioned that, upon the coordination of such diboron compounds with the surface oxygen atom in metal oxide materials, the formation of surface diboron-oxygen Lewis pair may induce single electron transfer from the *ipso*-O_{2c} site to the adjacent Ti site. Furthermore, the interaction of diboron species with the oxygen atom may stabilize the resulting low-valent Ti–high-valent O pair.

RESULTS AND DISCUSSION

Spectroscopic Characterizations

We use P25 TiO_2 to study the surface modification behavior, for P25 TiO_2 is typical TiO_2 material applied in photochemical applications and shows enhanced performance based on fine nanoparticles and heterointerface between anatase and rutile phases (Xia et al., 2013, 2014). Mechanical mixing of commercial Degussa TiO_2 P25 and bis(pinacolato)diboron (B_2Pin_2, **B1**) in a nitrogen-filled glovebox at room temperature resulted in a rapid color change from white to blue within 1 min (Figure 1E and Video S1). This blue titania, labeled as **B1**-TiO_2-N_2, was highly sensitive to O_2 and faded immediately upon exposure to air. Unexpectedly, heating **B1**-TiO_2-N_2 at 80°C under vacuum for 3 h resulted in a blue sample that is stable under air, which we labeled as **B1**-TiO_2. This sample could be stored outside the glovebox for weeks, and the blue color persisted. Similar transformations were observed with three other diboron compounds as shown in Figures 1 and S1. To fully disperse the diboron compound onto the TiO_2 nanoparticles, this heterogeneous reaction was performed in a diboron-soluble solvent, such as methanol or diethyl ether. Same blue samples were obtained after removal of organic solvents under vacuum. On the basis of previous studies (Iorio et al., 2012), the blue color was indicative of the formation of Ti^{3+} defects. To probe whether **B1** was oxidized in this process, the newly prepared blue **B1**-TiO_2 sample was extracted with $CDCl_3$, and **B1** was found to be the only boron-containing species present in the extract (Figure S2). Additionally, the use of this recovered **B1** from the extract for TiO_2 modification also gave rise to the same blue titania. Thus, these experiments suggested that diboron compound **B1** is not a one-off sacrifice agent. Based on these findings, a new mechanism must be responsible for the formation of this blue TiO_2.

To probe the existence of Ti^{3+} species, electron paramagnetic resonance (EPR) spectra (Zuo et al., 2010) of the **B1**-TiO_2 sample were acquired. Low-temperature (2 and 100 K) EPR data feature transitions with g = 1.97–1.99, whereas the room temperature EPR is silent (Figure 1F). This behavior is characteristic of Ti^{3+} species as documented by previous studies (Li et al., 2008). The observed g values show the presence of a strong anisotropic paramagnetic Ti^{3+} center, indicating that the local symmetry of Ti^{3+} is vastly broken. Furthermore, this Ti^{3+} EPR signal would be split if B replaces the bridging O or is directly bound to Ti (Gopal et al., 2008). However, in all the cw-EPR measurements, we did not observe the hyperfine coupling originating from the ^{10}B or ^{11}B nucleus. This suggests either no or very weak coupling between the B atom

[11]Beijing National Laboratory for Molecular Sciences, Key Laboratory of Photochemistry, CAS Research/Education Center for Excellence in Molecular Sciences, Institute of Chemistry, The Chinese Academy of Sciences, Beijing 100190, China

[12]These authors contributed equally

[13]Lead Contact

*Correspondence: fmo@pku.edu.cn

https://doi.org/10.1016/j.isci.2019.09.024

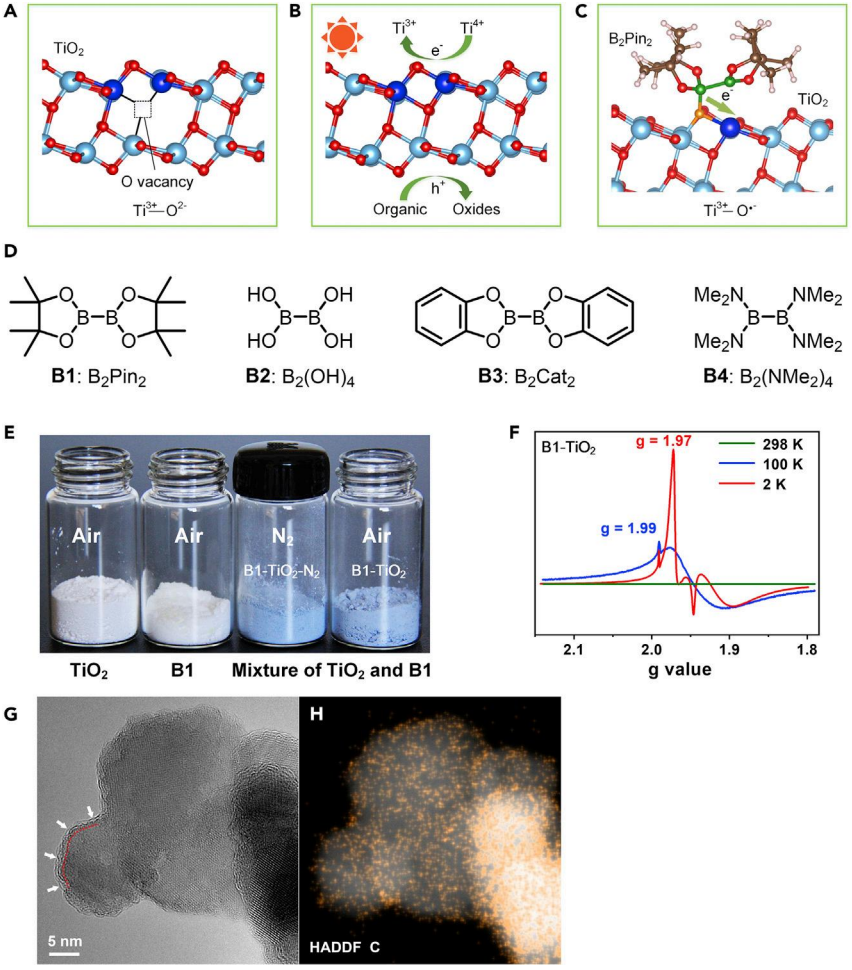

Figure 1. Conventional Methods and Present Work for the Preparation of Self-Doped Ti^{3+}-TiO_2 Materials

(A) Ti^{3+} generation as a result of oxygen vacancy formation. High-temperature combustion with reductant leads to oxygen vacancy in TiO_2 bulk phase (Zuo et al., 2010).

(B) Ti^{3+} generation by photo irradiation. By removal of photoinduced holes using organic sacrificial agents, electrons are cumulated at the conduction band of TiO_2, resulting in the reduction of Ti^{4+} to Ti^{3+} (Schrauben et al., 2012; Yan et al., 2017).

(C) Present work. Diboron compound (B_2Pin_2) adsorption on the surface of TiO_2 nanoparticles induces spontaneous electron injection for the formation of optically active Ti^{3+}—$O^{-\cdot}$ species. The light blue, blue, red, orange, earth yellow, green, and pink balls stand for the Ti^{4+}, Ti^{3+}, O^{2-}, $O^{-\cdot}$, C, B, and H atom, respectively.

(D) Four commercially available diboron compounds used in this study: B_2Pin_2 (bis(pinacolato)diboron), $B_2(OH)_4$ (tetrahydroxydiborane), B_2Cat_2 (bis(catecholato)diboron), and $B_2(NMe_2)_4$ (tetrakis(dimethylamino)diboron).

(E) Photograph comparing TiO_2 (P25), B_2Pin_2 (**B1**), **B1**-TiO_2-N_2 sample under an inert atmosphere (mixture of solid TiO_2 and B_2Pin_2) and **B1**-TiO_2 under air after heating at 80°C under vacuum for 3 h.

(F) EPR spectra of **B1**-TiO_2 at various temperatures.

(G) HRTEM of **B3**-TiO_2. A short-dashed curve is applied to outline a portion of the interface between the crystalline core and the outer layer (marked by white arrows).

(H) The corresponding HADDF-STEM image of **B3**-TiO_2 with distribution of the C element mapping.

and the Ti^{3+} center. Moreover, we found that **B3**-TiO_2 shows a *g* signal at 2.003 at room temperature (Figure S3), which could be characteristic of a Ti^{3+}-$O^{-\cdot}$ radical. We also applied the ACTEM method to study the existence and status of diboron molecule on the surface of TiO_2. In the high-resolution transmission electron microscopy (HRTEM) image of **B3**-TiO_2 (Figure 1G), we found that the surface of TiO_2 nanocrystal is wrapped by an outer layer with ~1-nm thickness. In addition, the EDS mapping of C element under the HADDF model (Figure 1H) shows a carbon-rich surface shell representing adsorbed organic diboron molecule on the TiO_2 surface.

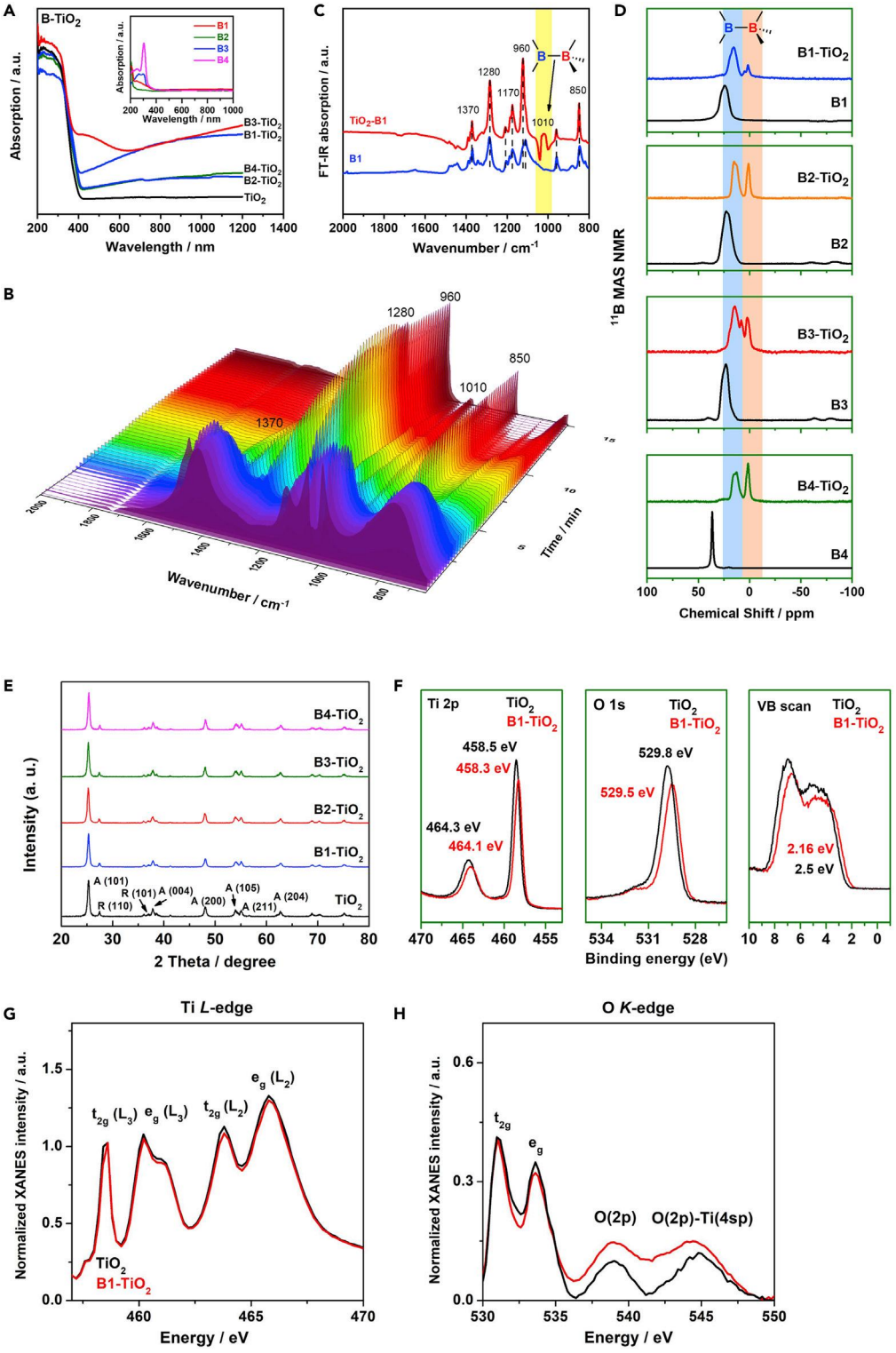

Figure 2. Spectroscopic Characterizations

(A) UV-vis spectra of the white TiO_2 P25 and diboron-adsorbed TiO_2 P25. The inset shows the UV-vis spectra of four free diboron compounds.

(B) *In situ* ATR-FTIR spectrum of **B1** onto TiO_2 over 15 min.

(C) FTIR spectra of free **B1** and **B1**-TiO_2.

Figure 2. *Continued*
(D) Solid-state ^{11}B MAS NMR of diboron compounds **B** and **B**-TiO_2.
(E) XRD pattern of the diboron compounds modified TiO_2.
(F) Ti 2p, O 1s, and valence band structure X-ray photoelectron spectroscopy spectra of TiO_2 and **B1**-TiO_2.
(G) Normalized Ti-*L* edge XANES spectra of TiO_2 and **B1**-TiO_2.
(H) Normalized O-*K* edge XANES spectra of TiO_2 and **B1**-TiO_2.

We next investigated the structures and properties of these diboron-TiO_2 nanoparticles with powder X-ray diffraction (PXRD), solid-state UV-vis spectroscopy (UV-vis), *in situ* attenuated total reflectance-Fourier transform infrared spectroscopy (*in situ* ATR-FTIR) and solid-state ^{11}B magic angle spinning nuclear magnetic resonance (^{11}B MAS NMR). PXRD analysis (Figure S4) shows that the commercial P25 sample is a mixture of anatase-phase and rutile-phase TiO_2. The PXRD pattern of TiO_2 remained the same upon adsorption of the diboron reagent, indicating that no phase change occurred in this process. Thus, this result suggests that the blue species is likely related to surface engineering rather than bulk phase modification. The solid-state UV-vis spectra in Figure 2A showed that neither the pristine white TiO_2 nor the diboron compound absorbs visible light (>400 nm). First, absorption bands beginning at 400 nm and steadily growing into the near-infrared (NIR) region were observed for all four **B**-TiO_2 samples. These adsorption bands were different from that arising from metal to ligand charge transfer of the surface complex between Ti^{4+} sites and organic ligands commonly observed in previous work (Lang et al., 2012). The UV-vis absorption spectra associated with Ti^{3+} materials can differ between different preparation methods (Howe and Gratzel, 1985). In our case, the diboron-modified TiO_2 samples were found to absorb visible light with higher intensity in the NIR region. This suggested that the Ti^{3+} species in our case is different from the previously reported Ti^{3+}-O^{2-} structures. In the *in situ* ATR-FTIR spectra (Figure 2B), the emergence of new signals corresponding to the diboron compound was observed over the time, clearly demonstrating the adsorption process. In the FTIR spectra (Figure 2C), signals at 1280 and 1170 cm^{-1} are assigned to two different types of B—O vibration. Based on density functional theory (DFT) calculations, the B—B stretching vibration appears at ca. 1000 cm^{-1} (Figure S5). As shown in Figure 2C, this signal is absent in **B1** owing to the C_2 symmetry of this diboron molecule. In contrast, a new peak at 1010 cm^{-1} corresponding to B—B stretching emerged in the **B1**-TiO_2 sample, thereby demonstrating the formation of the oxygen-diboron Lewis pair.

Solid-state ^{11}B MAS NMR spectroscopy was next used to elucidate the binding details of the diboron reagent with the TiO_2 surface. Upon adsorption, the B(sp^2)-B(sp^3) adducts should exhibit two distinct boron environments in the solid-state NMR spectra. As shown in Figure 2D, in all four cases, new peaks appear and shift upfield, indicating changes in the chemical environment of the two B atoms. Previous studies revealed that the ^{11}B signal of sp^3 hybridized tetracoordinate boron undergoes an upfield shift relative to the sp^2 hybridized tricoordinate one (Nöth and Wrackmeyer, 1978). Thus, we attribute the peaks close to 0 ppm to B atom bound to the surface O atom of TiO_2 nanoparticles. X-ray diffraction (XRD) was applied to examine the structure of the TiO_2 by diboron compound modification (Figure 2E). According to the XRD results, no change of the lattice was characterized. To further our understanding of the surface interaction between the diboron molecule and TiO_2 nanoparticles, we carried out XPS and SXANES studies. The Ti 2p spectra shows that the peaks were shifted for 0.2 eV toward the lower-binding-energy region; this also happened in O 1s spectra (Figure 2F). The valence band spectra show that the band level shifts to lower energy, a shift from 2.5 to 2.16 eV. The Ti 2p, O 1s spectra change means that the surface modification shows significant influence on the surface electron structure of the TiO_2. As shown in Figure 2G, the t_{2g} (L_3) peak of Ti-*L* edge shows that the **B1**-TiO_2 is slightly lower than that of pristine TiO_2 and the peak of e_g (L_2) is shifted to higher energy, which can be attributed to the existence of Ti^{3+} (Kronawitter et al., 2011; Stewart et al., 2006). The O-*K* edge originates from the hybridization of O_{2p} ligand-hole states with the coordinating atoms s, p, d states (Karvonen et al., 2010). In our case, the O-*K* edge shows that the peaks of **B1**-TiO_2 that index to the Ti–O bond around 545 eV and the O 2p around 539 eV are much higher than that of pristine TiO_2 (Figure 2H), demonstrating more electron location in O 2p orbital and Ti–O bond instead of the O e_g orbitals (de Groot et al., 1989). Meanwhile, the Ti-*K* edge line shows no significant change between **B1**-TiO_2 and pristine TiO_2 in the pre-edge region and the EXANE region (Figure S6). The reason is that the diboron compound is bonded with surface *ipso*-O^{2-} atoms. Moreover, the B 1s XPS also provides consistent results indexing of B species with different binding energies (Figure S7). On the basis of these spectroscopic evidences, we propose that the coordination of diboron compound with surface O sites on TiO_2 facilitates the electron transfer from the *ipso*-O^{2-} to the adjacent Ti^{4+} site and this coordination further stabilizes the newly formed Ti^{3+}-

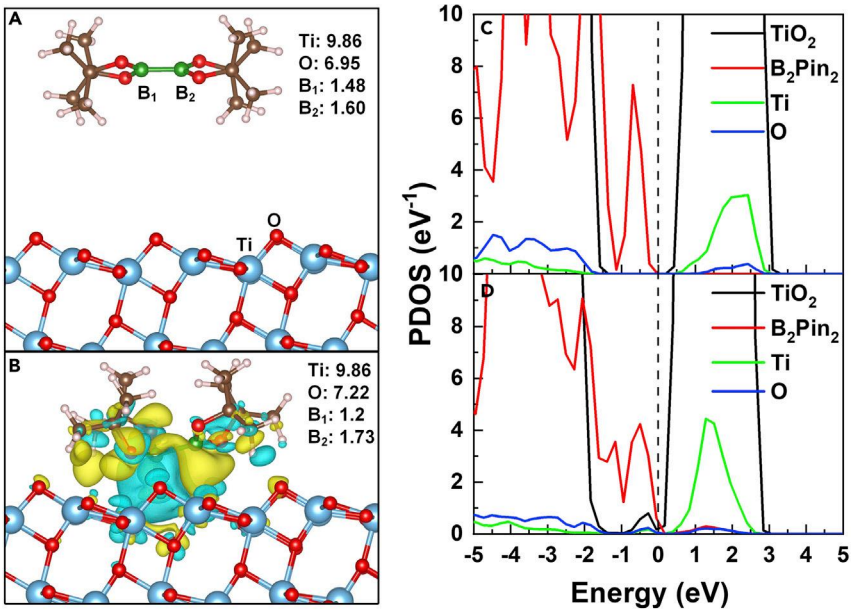

Figure 3. DFT Calculation Results

(A) Optimized geometric structures and charge difference density mappings for no adsorption.

(B) Optimized geometric structures and charge difference density mappings for adsorption of **B1** on the TiO_2 {101} surface. The numbers in the figure stand for the Bader charges on the various atoms. The isosurfaces of the electron density difference plots are all 0.001 e $Å^{-3}$. The yellow and light blue surfaces represent electron depletion and accumulation. The blue, red, earth yellow, green, and pink spheres stand for the Ti, O, C, B, and H atoms, respectively.

(C) Projected density of state (PDOS) plots for no adsorption.

(D) Projected density of state (PDOS) plots for adsorption of **B1** on the TiO_2 {101} surface (the insets on the right are the magnification of the inter band at near the Fermi energy level). The dashed line shows the Fermi level.

$O^{-\cdot}$ species. We note that the activation of inert lattice O^{2-} and the stabilization of surface Ti^{3+} enabled by the formation of $\equiv B–O^{-\cdot}–Ti^{3+}$ moiety is a novel process that has not been reported in TiO_2 modification.

DFT Calculation Results

We next investigated the surface $Ti^{3+}–O^{-\cdot}$ structure in the blue TiO_2 nanoparticles by simulating the adsorption of **B1** on the TiO_2 surface and the accompanying charge transfer between them using DFT calculations. According to the literature, the {101} facet in anatase TiO_2 is the dominant facet, and we set up the adsorption model of anatase TiO_2 {101} facet (Lazzeri et al., 2001). Our calculations showed that the Fermi levels in no adsorption is located in the TiO_2 band gap (Figures 3A and 3C). Importantly, the diboron-adsorbed TiO_2 model shows a clear charge transfer from **B1** to the TiO_2 {101} surface (Figure 3B). Furthermore, the Bader charge calculation showed substantial electron transfer from the B_1 atom to the bridging O atom. Furthermore, those electrons (light blue region) are localized between the bridging O atom and the neighbor surface Ti atom according to the calculated charge difference density mapping. The calculated projected density of state (PDOS) plots showed that the Fermi level rises to the bottom of the TiO_2 conduction band, which is mainly derived from Ti 3d states (Figure 3D). Some Ti 3d and O 2p states below the Fermi level appear, which are filled with electrons. The filled Ti 3d states indicate the partial reduction of the surface Ti sites, which explains the existence of the Ti^{3+} species observed in our EPR experiments. Moreover, the adsorption model of **B2**, **B3**, and **B4** on TiO_2 {101} surface was also calculated (Figures S8A–S8C and S9). These data showed that a new electron-filled band-gap state consisting of Ti 3d appears in all the three models (Figures S8D–S8F and S9). This strongly suggested that the adsorption of organic diboron compounds can lead to the formation of Ti^{3+} species on the TiO_2 surface. The adsorption model based on rutile TiO_2 shows similar results (Figures S10 and S11). The adsorption model of the interface between anatase TiO_2 and rutile TiO_2 was also set up to evaluate the heterojunction in P25 nanoparticles (Figures S12 and S13). To interpret the stability of the surface Ti^{3+} in B-TiO_2 in the air atmosphere, the oxygen adsorption models were set. The calculation result shows that O_2 molecule is

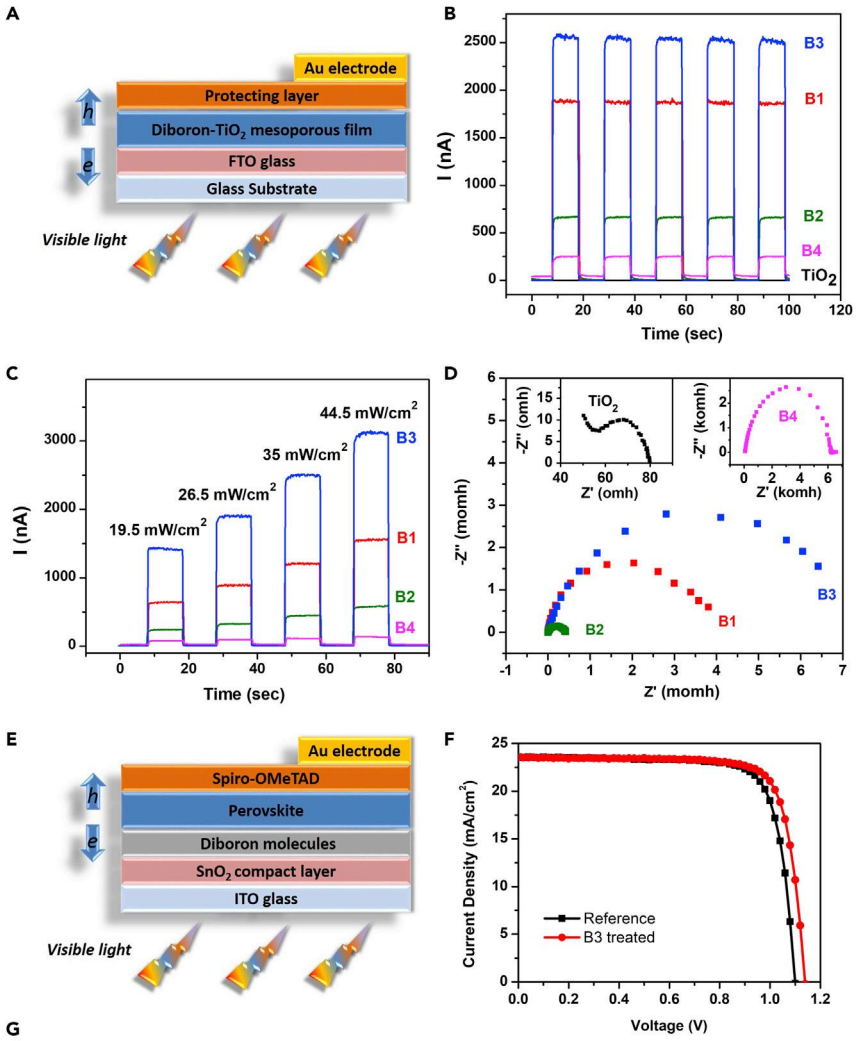

G

	Voc (V)	Jsc (mA/cm²)	FF (%)	PCE (%)
Reference	1.105	23.46	79.45	20.60
B3 treated	1.143	23.35	80.32	21.44

Figure 4. Photodetectors and Perovskite Solar Cells Performance

(A) Schematic of the FTO/TiO_2/diboron/Spiro-OMeTAD/Au photodetector.

(B) Time-dependent current curves for the detectors under light illumination ($\lambda > 400$ nm) with 10 s on-off switching intervals.

(C) Time-dependent current curves for these photodetectors under illumination intensities ($\lambda > 400$ nm) of 19.5, 26.5, 35.0, and 44.5 $mW \cdot cm^{-2}$.

(D) Nyquist plots from the photodetectors in the dark.

(E) Schematic of the ITO/SnO_2/diboron/Perovskite/Spiro-OMeTAD/Au solar cell.

(F) Current density-voltage curves (*J-V*) of the diboron-modified perovskite solar cell.

(G) Photovoltaic parameters of the diboron-modified perovskite solar cell. FF, fill factor; PCE, power conversion efficiency.

hesitant to adsorb to the adjacent Ti_{5c} site of the molecule (energy rising process), which represents the protection role of the molecule (Figure S14 and Table S1).

Photodetectors and Perovskite Solar Cells Performance

To further explore the optoelectronic properties of this diboron-adsorbed TiO_2 material under visible-light excitation, thin films were then fabricated into photodetectors (denoted as FTO/TiO_2/diboron/Spiro-OMeTAD/Au, Figure 4A). The time-dependent current curves (*I-t*) for these diboron-type

photodetectors under visible-light illumination (>400 nm) exhibited excellent on-off switching repetitions through five cycles (interval = 10 s) (Figure 4B). The photocurrent for these four diboron-type detectors increased linearly with the light intensity (Figures 4C and S15 and Table S2). In contrast, the observed photocurrent for TiO_2 without diboron modification did not change regardless of the on-off state, which was ascribed to the intrinsic band gap of anatase TiO_2 (3.2 eV). Furthermore, the charge transport process in diboron-modified devices was investigated using electrochemical impedance spectroscopy measurements in the dark at 0 V (Figure 4D). The larger semicircle radius of Nyquist plot in the low-frequency region for the **B3** device compared with the **B1**, **B2**, and **B4** devices indicated less electron recombination (Kim et al., 2012). This observation agreed well with the highest photocurrent for the **B3** device (Figure 4B). The IPCE (incident photon-to-electron conversion efficiency) was also evaluated, and the **B3**-TiO_2 device shows the best performance (Figure S16). The **B**-TiO_2 photodetectors show good response toward long-time on-off tests compared with the TiO_2 photodetector (Figures S17 and S18), and the response of the photodetectors does not attenuate after being stored in a dry air atmosphere for at least 7 months (Figure S19). We also fabricated solar cells based on the diboron molecule interface modulation, and the *J-V* performance of the device was characterized showing an improved solar cell performance (Figures 4E–4G). The data show that the **B3**-treated device based on the **B3**-SnO_2 interface has a better performance compared with the reference device of SnO_2-based perovskite solar cell.

We note that previously developed solar cells such as dye-sensitized solar cells and perovskite solar cells inevitably involve the use of expensive dyes and/or toxic and unstable reagents. Thus, our approach to generating visible-light active center via the adsorption of stable and inexpensive diboron compounds holds great advantages over these traditional techniques. Furthermore, a diverse range of diboron compounds can be conveniently synthesized from **B4**, potentially allowing for the fine-tuning of semiconductor-based materials. More importantly, the present strategy is not limited to TiO_2. In our studies, we have determined that a broad range of other common semiconducting oxides, including ZnO, SnO_2, Nb_2O_5, and In_2O_3, were also successfully modified by diboron reagents, thus clearly demonstrating the generality of this method for semiconducting metal oxide modification (Figure S20).

Limitations of the Study

In the current study, perovskite solar cells assembled from **B**-TiO_2 display relatively poor performance (Figure S21). Many factors such as device fabrication could influence the performance of such device. Additionally, in our present work, mesoporous TiO_2 was used in **B**-TiO_2-based devices, whereas planar SnO_2 was used in **B**-SnO_2-based devices. We are uncertain if this deviation led to the contrasting device performance based on **B**-TiO_2 and **B**-SnO_2 materials. Nonetheless, the three orders of magnitude improvement observed in the **B**-TiO_2-based photodetector clearly demonstrates the utility of this diboron-based modification strategy. Currently, we are actively pursuing other applications based on diboron-modified semiconductor oxide materials featuring unique surface defects.

METHODS

All methods can be found in the accompanying Transparent Methods supplemental file.

SUPPLEMENTAL INFORMATION

Supplemental Information can be found online at https://doi.org/10.1016/j.isci.2019.09.024.

ACKNOWLEDGMENTS

We thank J. C. Zhao for encouragement; H. J. Yang (Tsinghua University), G. Q. Liu (Peking University), S. L. Wang (Peking University), H. P. Zhou (Peking University), and L. Jiao (Tsinghua University) for insightful discussions; H. Fu (Peking University), H. J. Yang and X. Zhang (Peking University) for assistance with ^{11}B MAS NMR spectroscopy. A portion of the EPR work was performed on the Steady High Magnetic Field Facilities, High Magnetic Field Laboratory of Chinese Academy of Sciences. The authors thank beamline BL08U1A and BL14W1 (Shanghai Synchrotron Radiation Facility) for providing the beam time. This research was supported by the National Natural Science Foundation of China (21772003, 91733301, and 91433203), the 973 Program of China (2015CB932203), ENN Group, and BHP-PKU CCUS project.

AUTHOR CONTRIBUTIONS

F.M. conceived the idea. Y.C., P.Z., Y.T., Z.L., and B.-W.D. performed experiments. Y.C., P.Z., and X.Z. conducted the DFT calculation. All authors analyzed data. Y.C., P.Z., Y.T., X.Z., Y.Y., S.-D.J., F.M., and W.M. wrote the manuscript. F.M. directed the whole project.

DECLARATION OF INTERESTS

The authors declare no competing interests.

Received: June 25, 2019
Revised: September 1, 2019
Accepted: September 13, 2019
Published: October 25, 2019

REFERENCES

Asahi, R., Morikawa, T., Irie, H., and Ohwaki, T. (2014). Nitrogen-doped titanium dioxide as visible-light-sensitive photocatalyst: designs, developments, and prospects. Chem. Rev. *114*, 9824–9852.

Asahi, R., Morikawa, T., Ohwaki, T., Aoki, K., and Taga, Y. (2001). Visible-light photocatalysis in nitrogen-doped titanium oxides. Science *293*, 269–271.

Chen, X., and Burda, C. (2008). The electronic origin of the visible-light absorption properties of C-, N- and S-doped TiO2 nanomaterials. J. Am. Chem. Soc. *130*, 5018–5019.

Chen, X., Liu, L., Yu, P.Y., and Mao, S.S. (2011). Increasing solar absorption for photocatalysis with black hydrogenated titanium dioxide nanocrystals. Science *331*, 746–750.

Chen, X., and Mao, S.S. (2007). Titanium dioxide nanomaterials: synthesis, properties, modifications, and applications. Chem. Rev. *107*, 2891–2959.

Dahl, M., Liu, Y., and Yin, Y. (2014). Composite titanium dioxide nanomaterials. Chem. Rev. *114*, 9853–9889.

de Groot, F.M.F., Grioni, M., Fuggle, J.C., Ghijsen, J., Sawatzky, G.A., and Petersen, H. (1989). Oxygen 1s x-ray-absorption edges of transition-metal oxides. Phys. Rev. B *40*, 5715–5723.

Gopal, N.O., Lo, H.-H., and Ke, S.-C. (2008). Chemical state and environment of boron dopant in B,N-codoped anatase TiO2 nanoparticles: an avenue for probing diamagnetic dopants in TiO2 by electron paramagnetic resonance spectroscopy. J. Am. Chem. Soc. *130*, 2760–2761.

Grätzel, M. (2001). Photoelectrochemical cells. Nature *414*, 338.

Green, M., Liu, Z., Xiang, P., Liu, Y., Zhou, M., Tan, X., Huang, F., Liu, L., and Chen, X. (2018a). Doped, conductive SiO2 nanoparticles for large microwave absorption. Light Sci. Appl. *7*, 87.

Green, M.A., Xu, J., Liu, H., Zhao, J., Li, K., Liu, L., Qin, H., Zhu, Y., Shen, D., and Chen, X. (2018b). Terahertz absorption of hydrogenated TiO2 nanoparticles. Mater. Today Phys. *4*, 64–69.

Green, M., Van Tran, A.T., Smedley, R., Roach, A., Murowchick, J., and Chen, X. (2019a). Microwave absorption of magnesium/hydrogen-treated titanium dioxide nanoparticles. Nano Mater. Sci. *1*, 48–59.

Green, M., Xiang, P., Liu, Z., Murowchick, J., Tan, X., Huang, F., and Chen, X. (2019b). Microwave absorption of aluminum/hydrogen treated titanium dioxide nanoparticles. J. Materiomics *5*, 133–146.

Guan, L., and Chen, X. (2018). Photoexcited charge transport and accumulation in anatase TiO2. ACS Appl. Energy Mater. *1*, 4313–4320.

Hoffmann, M.R., Martin, S.T., Choi, W., and Bahnemann, D.W. (1995). Environmental applications of semiconductor photocatalysis. Chem. Rev. *95*, 69–96.

Howe, R.F., and Gratzel, M. (1985). EPR observation of trapped electrons in colloidal titanium dioxide. J. Phys. Chem. *89*, 4495–4499.

Iorio, Y.D., Aguirre, M.E., Brusa, M.A., and Grela, M.A. (2012). Surface chemistry determines electron storage capabilities in alcoholic sols of titanium dioxide nanoparticles. a combined FTIR and room temperature EPR investigation. J. Phys. Chem. C *116*, 9646–9652.

Karvonen, L., Valkeapää, M., Liu, R.-S., Chen, J.-M., Yamauchi, H., and Karppinen, M. (2010). O-K and Co-L XANES study on oxygen intercalation in perovskite SrCoO3-δ. Chem. Mater. *22*, 70–76.

Khan, S.U.M., Al-Shahry, M., and Ingler, W.B. (2002). Efficient photochemical water splitting by a chemically modified n-TiO2. Science *297*, 2243–2245.

Kim, K.S., Song, H., Nam, S.H., Kim, S.-M., Jeong, H., Kim, W.B., and Jung, G.Y. (2012). Fabrication of an efficient light-scattering functionalized photoanode using periodically aligned ZnO hemisphere crystals for dye-sensitized solar cells. Adv. Mater. *24*, 792–798.

Kronawitter, C.X., Bakke, J.R., Wheeler, D.A., Wang, W.-C., Chang, C., Antoun, B.R., Zhang, J.Z., Guo, J., Bent, S.F., Mao, S.S., et al. (2011). Electron enrichment in 3d transition metal oxide hetero-nanostructures. Nano Lett. *11*, 3855–3861.

Lang, X., Ma, W., Zhao, Y., Chen, C., Ji, H., and Zhao, J. (2012). Visible-light-induced selective photocatalytic aerobic oxidation of amines into imines on TiO2. Chem. Eur. J. *18*, 2624–2631.

Lazzeri, M., Vittadini, A., and Selloni, A. (2001). Structure and energetics of stoichiometric TiO2 anatase surfaces. Phys. Rev. B *63*, 155409.

Li, G., Dimitrijevic, N.M., Chen, L., Nichols, J.M., Rajh, T., and Gray, K.A. (2008). The important role of tetrahedral Ti4+ sites in the phase transformation and photocatalytic activity of TiO2 nanocomposites. J. Am. Chem. Soc. *130*, 5402–5403.

Liu, L., and Chen, X. (2014). Titanium dioxide nanomaterials: self-structural modifications. Chem. Rev. *114*, 9890–9918.

Liu, Q., Hong, J., Sun, B., Bai, G., Li, F., Liu, G., Yang, Y., and Mo, F. (2019). Transition-metal-free borylation of alkyl iodides via a radical mechanism. Org. Lett. *21*, 6597–6602.

Maeda, K., Teramura, K., Lu, D., Takata, T., Saito, N., Inoue, Y., and Domen, K. (2006). Photocatalyst releasing hydrogen from water. Nature *440*, 295.

Mo, F., Jiang, Y., Qiu, D., Zhang, Y., and Wang, J. (2010). Direct conversion of arylamines to pinacol boronates: a metal-free borylation process. Angew. Chem. Int. Ed. *49*, 1846–1849.

Mo, F., Qiu, D., Zhang, Y., and Wang, J. (2018). Renaissance of Sandmeyer-type reactions: conversion of aromatic C–N bonds into C–X bonds (X = B, Sn, P, or CF3). Acc. Chem. Res. *51*, 496–506.

Neeve, E.C., Geier, S.J., Mkhalid, I.A.I., Westcott, S.A., and Marder, T.B. (2016). Diboron(4) compounds: from structural curiosity to synthetic workhorse. Chem. Rev. *116*, 9091–9161.

Nöth, H., and Wrackmeyer, B. (1978). 11B NMR of tetracoordinate boron. In Nuclear Magnetic Resonance Spectroscopy of Boron Compounds, H. Nöth and B. Wrackmeyer, eds. (Springer Berlin Heidelberg), pp. 74–101.

Pietsch, S., Neeve, E.C., Apperley, D.C., Bertermann, R., Mo, F., Qiu, D., Cheung, M.S., Dang, L., Wang, J., Radius, U., et al. (2015). Synthesis, structure, and reactivity of anionic sp2–sp3 diboron compounds: readily accessible boryl nucleophiles. Chem. Eur. J. *21*, 7082–7098.

Schrauben, J.N., Hayoun, R., Valdez, C.N., Braten, M., Fridley, L., and Mayer, J.M. (2012). Titanium and zinc oxide nanoparticles are proton-coupled electron transfer agents. Science *336*, 1298–1301.

Stewart, S.J., Fernández-García, M., Belver, C., Mun, B.S., and Requejo, F.G. (2006). Influence of N-doping on the structure and electronic properties of titania nanoparticle photocatalysts. J. Phys. Chem. B *110*, 16482–16486.

Tian, L., Xu, J., Alnafisah, A., Wang, R., Tan, X., Oyler, N.A., Liu, L., and Chen, X. (2017). A novel green TiO2 photocatalyst with a surface charge-transfer complex of Ti and hydrazine groups. Chem. Eur. J. *23*, 5345–5351.

Wang, D., Kako, T., and Ye, J. (2008). Efficient photocatalytic decomposition of acetaldehyde over a solid-solution perovskite (Ag0.75Sr0.25)(Nb0.75Ti0.25)O3 under visible-light irradiation. J. Am. Chem. Soc. *130*, 2724–2725.

Wang, G., Zhang, H., Zhao, J., Li, W., Cao, J., Zhu, C., and Li, S. (2016). Homolytic cleavage of a B—B bond by the cooperative catalysis of two Lewis bases: computational design and experimental verification. Angew. Chem. Int. Ed. *55*, 5985–5989.

Xia, T., Li, N., Zhang, Y., Kruger, M.B., Murowchick, J., Selloni, A., and Chen, X. (2013). Directional heat dissipation across the interface in anatase-rutile nanocomposites. ACS Appl. Mater. Interfaces *5*, 9883–9890.

Xia, T., Zhang, Y., Murowchick, J., and Chen, X. (2014). Vacuum-treated titanium dioxide nanocrystals: optical properties, surface disorder, oxygen vacancy, and photocatalytic activities. Catal. Today *225*, 2–9.

Yan, Y., Shi, W., Yuan, Z., He, S., Li, D., Meng, Q., Ji, H., Chen, C., Ma, W., and Zhao, J. (2017). The formation of Ti–H species at interface is lethal to the efficiency of TiO2-based dye-sensitized devices. J. Am. Chem. Soc. *139*, 2083–2089.

Zhang, L., and Jiao, L. (2017). Pyridine-catalyzed radical borylation of aryl halides. J. Am. Chem. Soc. *139*, 607–610.

Zuo, F., Wang, L., Wu, T., Zhang, Z., Borchardt, D., and Feng, P. (2010). Self-doped Ti3+ enhanced photocatalyst for hydrogen production under visible light. J. Am. Chem. Soc. *132*, 11856–11857.

ISCI, Volume *20*

Supplemental Information

Modification of TiO_2 Nanoparticles with Organodiboron Molecules Inducing Stable Surface Ti^{3+} Complex

Yang Cao, Peng Zhou, Yongguang Tu, Zheng Liu, Bo-Wei Dong, Aryan Azad, Dongge Ma, Dong Wang, Xu Zhang, Yang Yang, Shang-Da Jiang, Rui Zhu, Shaojun Guo, Fanyang Mo, and Wanhong Ma

Supplementary Materials

This PDF file includes:

Transparent Methods

EXPERIMENTAL PROCEDURES

Sample preparations

B1-TiO_2-N_2 sample: In a glovebox, 50 mg B_2Pin_2 was dissolved in 2 mL dry CH_3OH. Then 0.5 g TiO_2 (Degussa P25, 20 nm) was added into the solution. The mixture was stirred for overnight at room temperature. After evaporation of the solvent by an oil pump, the titled sample was obtained as a blue powder. This blue titania is sensitive to oxygen and will fade when exposed to air. However, when the sample is again isolated from air, the blue color returns. By the same procedure, the corresponding **B2**-TiO_2-N_2, **B3**-TiO_2-N_2, **B4**-TiO_2-N_2 were prepared from **B2** $B_2(OH)_4$, **B3** B_2Cat_2, **B4** $B_2(NMe_2)_4$, respectively.

B1-TiO_2 sample: This sample was obtained by heating the above sample at 80 ^oC under high vacuum for 3 h. **B2**-TiO_2, **B3**-TiO_2 and **B4**-TiO_2 were obtained by the same procedure.

Device Fabrication

Photodetector fabrication:

The pre-patterned FTO substrates (NSG) were cleaned by UV-ozone treatment for 15 min, followed by cleaning ultrasonically with deionized water, detergent, acetone, and isopropanol in succession for 20 min. A 30 nm TiO_2 compact layer was deposited on the pre-cleaned FTO glass by spray pyrolysis using O_2 as the carrying gas at 450 ^oC from a precursor solution of 0.6 mL titanium diisopropoxide bis(acetylacetonate) and 0.4 mL acetylacetonate in 9 mL anhydrous ethanol. A 150 nm mesoporous TiO_2 was coated on the substrate by spin-coating with a speed of 5000 rpm for 10 s with a ramp rate of 2000 rpm s^{-1}, from a diluted 30 nm TiO_2 particle paste (Dyesol 30 NR-D) in ethanol with the weight ratio of TiO_2 paste/ethanol = 1:6, and then the substrate was sintered at 500 ^oC for 30 min. For the adsorption of diboron compounds, the mesoporous TiO_2 films were immersed in 5 mg mL^{-1} B_2Pin_2, B_2Cat_2, $B_2(OH)_4$ in anhydrous isopropanol at room temperature for 24 h in the nitrogen glove box, respectively. Then the diboron-sensitized TiO_2 films were heated

at 100 °C for 5 min. For the sample of $B_2(NMe_2)_4$-sensitized TiO_2 films, $B_2(NMe_2)_4$ solvent was spin-coated on the TiO_2 film with a speed of 2500 rpm for 20 s, then annealed at 40 °C for 2 min to remove extra solvent. The amount of diboron compounds on each film were examined by ICP method (Table S3). After cooling down to room temperature, 2,2',7,7'-tetrakis(*N,N*-di-pmethoxyphenylamine)-9,9'-spirobifluorene (spiro-OMeTAD) solution was spin-coated onto the active layer at 4000 rpm for 30 s. A spiro-OMeTAD solution was prepared by dissolving 72.3 mg of spiro-OMeTAD in 1 mL of chlorobenzene, to which 28.8 mL of 4-tert-butyl pyridine and 17.5 mL of lithium bis(trifluoromethanesulfonyl)imide (Li-TFSI) solution (520 mg LI-TSFI in 1 mL acetonitrile) were added. All devices were stored in a desiccator (humidity < 15 %) for 12 h. Finally, 80 nm of gold was deposited under vacuum through a shadow mask.

Solar cell fabrication:

SnO_2-based perovskite solar cells fabrication. The ITO substrates were cleaned with ultrapure water, acetone, ethanol and isopropanol subsequently. The cleaned ITO substrates were treated under ozone irradiation for 45 min. Then the subsequent were coated with a SnO_2 nanocrystal solution at 4000 rpm/min for 30 second forming a 50 nm thick layer, then annealed at 150 °C for 30 min in air atmosphere. Then 0.1 mM B3 DMF solution were spin coated onto the layer for 5000 rpm for 30 second in N_2 atmosphere, then annealed at 70 °C for 5 min. The perovskite film was fabricated by a two-step solution process: the 1.3 M PbI_2 in DMF/DMSO (9:1) mixture were spin-coated on the ITO substrate for 2500 rpm/min for 30 second, then annealed for 1 min at 70 °C in N_2 glovebox. A mixed organic cation isopropanol solution (MAI 0.12 M; MABr 0.05 M; MACl 0.07 M; FAI 0.23 M) were spin coated for 30 second at 2300 rpm/min and subsequent annealation at 150 °C. Then a spiro-OMeTAD/chlorobenzene solution including 35 μL Li-TFSI/acetonitrile, 30 μL 4-tertbutylpyridine, was coated onto the perovskite layer with 3500 rpm/min for 30 second. After that, 80 nm Au were deposit onto the substrate by thermo evaporation method. The fabricated solar cell was stored in a desiccator (humidity < 15 %) for 12 h before performance measurement.

TiO_2-based perovskite solar cells fabrication. The pre-patterned FTO substrates (NSG) were cleaned by UV-ozone treatment for 15 min, followed by cleaning ultrasonically with deionized water, detergent, acetone, and isopropanol in succession for 20 min. A 30

nm TiO_2 compact layer was deposited on the pre-cleaned FTO glass by spray pyrolysis using O_2 as the carrying gas at 450 °C from a precursor solution of 0.6 mL titanium diisopropoxide bis(acetylacetonate) and 0.4 mL acetylacetonate in 9 mL anhydrous ethanol. A 150 nm mesoporous TiO_2 was coated on the substrate by spin-coating with a speed of 5000 rpm for 10 s with a ramp rate of 2000 rpm s^{-1}, from a diluted 30 nm TiO_2 particle paste (Dyesol 30 NR-D) in ethanol with the weight ratio of TiO_2 paste/ethanol = 6:1, and then the substrate was sintered at 500 °C for 30 min. After cooling down to room temperature, 5 mg mL^{-1} B_2Pin_2 in anhydrous isopropanol was spin-coated onto the TiO_2 film with a speed of 2000 rpm for 20 s in N_2 atmosphere, then annealed 100 °C for 5 min. The cesium-containing triple cation perovskite precursor solution was prepared by mixing PbI_2 (1.15 M), FAI (1.09 M), $PbBr_2$ (0.20 M), MABr (0.14 M) and CsI (0.06 M) in a mixed solvent of DMF/DMSO/NMP (DMF/DMSO, 4/1, v/v) and stirred at 70 °C for 10 min before use. The perovskite solution was deposited on TiO_2 substrate with two-step program: 2000 rpm for 10 s with a ramping up speed of 2000 rpm/s, and 6000 rpm for 30 s with a ramping up speed of 2000 rpm/s, respectively. 100 μL of chlorobenzene was poured on the center of the spinning substrate during the spin-coating step at 15 s before the end of the procedure. The substrate was then immediately transferred on a hot plate and heated at 100 °C for 1 h. After cooling down to room temperature, 20 μL of 60 mM Spiro-OMeTAD solution was spin-coated on the perovskite layer at 4000 rpm for 30 s. A Spiro-OMeTAD solution was prepared by dissolving 72.3 mg of Spiro-OMeTAD in 1 mL of chlorobenzene, to which 28.8 μL of 4-tert-butyl pyridine and 17.5 μL of lithium bis(tri-uoromethanesulfonyl)imide (Li-TFSI) solution (520 mg LI-TSFI in 1 mL acetonitrile) were added. All devices were stored in a desiccator (humidity < 15%) in the dark for 12 h. Finally, 80 nm of gold was deposited under vacuum through a shadow mask to ensure the same active layer area (0.0863 cm^2).

Materials and Methods

The characterization details:

Electron paramagnetic resonance was collected on a Bruker EMX plus under continuous wave model of X wave at room temperature or low temperature hold by liquid Helium.

FT-IR spectroscopy were collected on a Thermal Nicolet iS 50 spectrometer equipped with a MCT detector with high resolution, which is cooled to 77 K by liquid N_2 during the detecting period. For each sample, the data were collected for 128 scans at 4 cm^{-1} resolutions. Solid-state ^{11}B NMR spectra were performed on a JEOL JNM-ECZ600R NMR spectrometer (14.1 T) equipped with a 3.2 mm probe at room temperature. The corresponding ^{11}B Larmor frequency is 192.4 MHz. A standard solid single pulse sequence was employed, and the $\tau/2$ pulse widths was 4 μs. The ^{11}B NMR experiments were carried out with an effective sample volume of 50 μL and a sample spinning rate of about 20 kHz. Chemical shifts are referenced to 0.1 M $B(OH)_3$ in D_2O at 19.6 ppm, solid $NaBH_4$ at -42.1 ppm. All spectra were acquired using 1024 scans with a recycle delay time of 5s. The collected NMR data were processed using Delta software. X-ray diffraction spectra were collected on a Rigaku RINT 2000 spectrometer. Photo detection measurement were performed on a CHI 670E electrochemical workstation from Shanghai Chen Hua Company. The light source was irradiated from a 300 W solar simulator from Newport Company with a 400 nm cut off. Impedance spectroscopy measurements were carried out by CHI670E electrochemical workstation. Solid state UV-VIS-NIR spectrograph were collected on a UV-3600 plus Shimadzu UV-VIS-NIR spectroscopy. XPS spectra were collected on a Thermo Scientific Escalab 250Xi spectrometer.

The XAS measurements of the TiO_2 and diboron modified TiO_2 sample were operated in transmittance mode at the XAS beamline of BL14W of Shanghai Synchrotron Source (3.5 GeV). The energy range of the beamline were 4 to 15 keV. The collect data were fitted using the ATHENA software package. The test sample were prepared by mixing of 50 mg LiF and 7 mg TiO_2 or **B**-TiO_2 and then press to a tablet. A Si (311) monochromator were used to collect the data and the energy were calibrated by using a Ti metal foil. We collect the Ti K line data around 4966 eV.

The Ti L line and O K line were collected on the BL08U1 of Shanghai Synchrotron Source. Boron K-edges, oxygen K-edges, Titanium L-edges sXANES spectra were collected in total electron yield (TEY) mode at beamline 08U1A of Shanghai Synchrotron Radiation Center. The spectra were calibrated with a clean gold mesh which give a simultaneous photocurrent based on the photon flux.

ATR-FTIR measurements:

The ATR- FTIR measurements were performed on a Nicolet 6700 FTIR instrument with a mercury cadmium telluride (MCT) detector. IR spectra ranging from 4000 to 1000 cm^{-1} were recorded by averaging 32 scans with a resolution of 4 cm^{-1}. The TiO_2 film was coated on a ZnSe crystal. 2 mL of methanol was dripped onto the film surface and then purged with Ar for 5 min at a flow rate of 20 mL min^{-1}. After adsorption equilibrium was achieved, the background spectrum was collected. Then a B_2Pin_2-containing methanol solution was added and the corresponding IR spectrum was recorded.

Computational details:

The electronic properties of the no adsorption and adsorption models of **B1** on the TiO_2 {101} surface were investigated using the Vienna Ab-initio Simulation Package (VASP). The Perdew-Burke-Ernzerhof (PBE) of the generalized gradient approximation (GGA) was used as the exchange-correlation function (Perdew et al., 1996; Perdew and Wang, 1992). The interaction between the valence electrons and the ionic core was described by the PAW pseudo-potential. The anatase TiO_2 {101} facet is a typical model used to simulate the TiO_2 crystal surface. The interactions between the two adjacent **B1** molecules on the periodic TiO_2 surface were modeled using one 2 × 4 {101} supercell with four O−Ti−O layers (Figure 3a and 3b). Two models were optimized with adsorption and without adsorption. Considering the balance between the supercell size and the calculational cost, the geometry was only optimized at the gamma point. The energy cutoff of the plane-wave basis was set to 350 eV and the energy convergence was set to 1.0×10^{-4} eV. The interactions between the two adjacent **B1** molecules on the periodic rutile {110} TiO_2 surface were modeled using one 2 × 4 {110} supercell with four O−Ti−O layers. The heterojunction adsorption model by joining anatase {112} and rutile {101} of 8A/3R (phase ratio of anatase/rutile phase: 8/3) were also modeled to simulate the adsorption on the heterojunction region.(Zhao et al., 2015) The adsorption energy (E_{ads}) of the **B1** molecules adsorbed on the TiO_2 {101} surface was calculated using Equation (1) where E_{total} is the total energy of the **B1**-adsorbed TiO_2 {101} surface, $E(TiO_2)$ is the free energy of the TiO_2 {101} surface, and E(**B1**) is the free energy of one **B1** molecule in vacuum.

$$E_{ads} = E_{total} - E(TiO_2) - E(\mathbf{B1}) \quad (1)$$

After the geometry optimization, the Monkhorst-Pack 2 × 2 × 1 k-point mesh was used for the partial density of state (PDOS) calculations for the optimized adsorption models. The charge difference density mapping and the bader charge were also calculated to investigate the charge transfer between the **B1** and the TiO_2 surface.

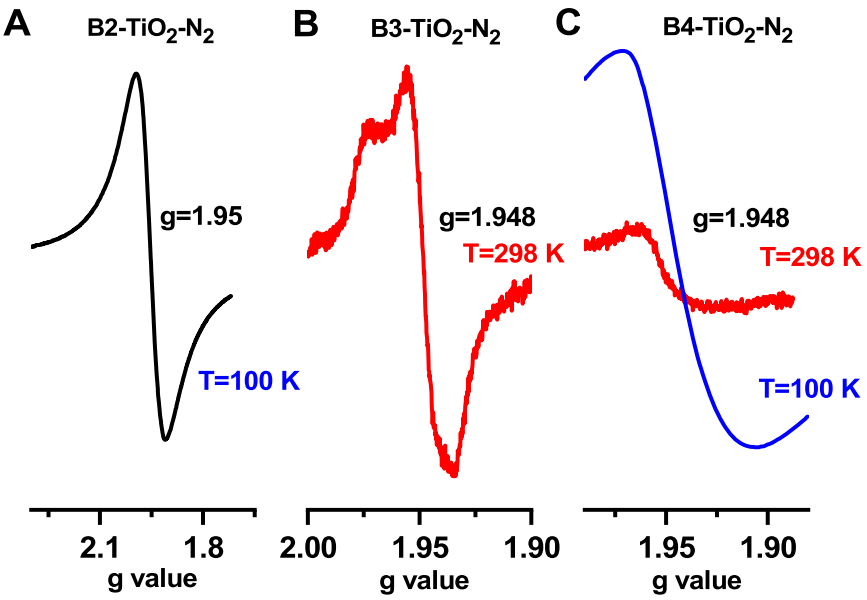

Figure S1. EPR signal of (A) **B2**-TiO_2-N_2 (B) **B3**-TiO_2-N_2 (C) **B4**-TiO_2-N_2 at room temperature or 100 K (The sample were protected under N_2 atmosphere during measurement). Related to Figure 1.

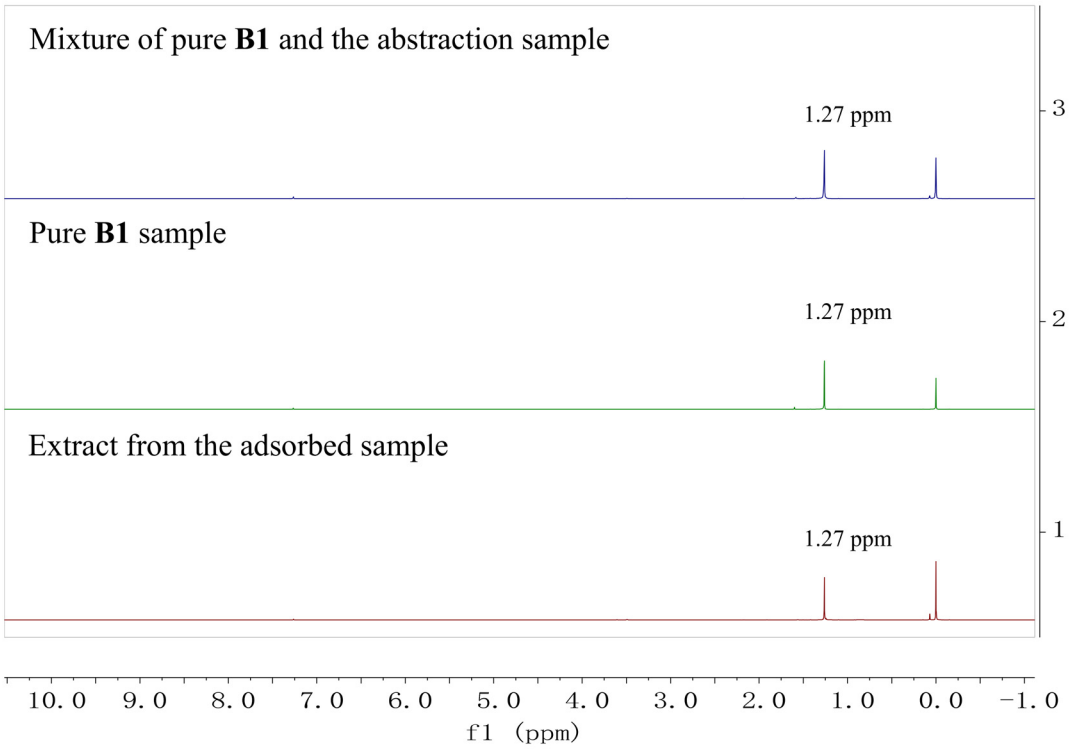

Figure S2. ^{1}H NMR spectra indicate that **B1** is unchanged upon extraction from the adsorbed sample. Related to Figure 1.

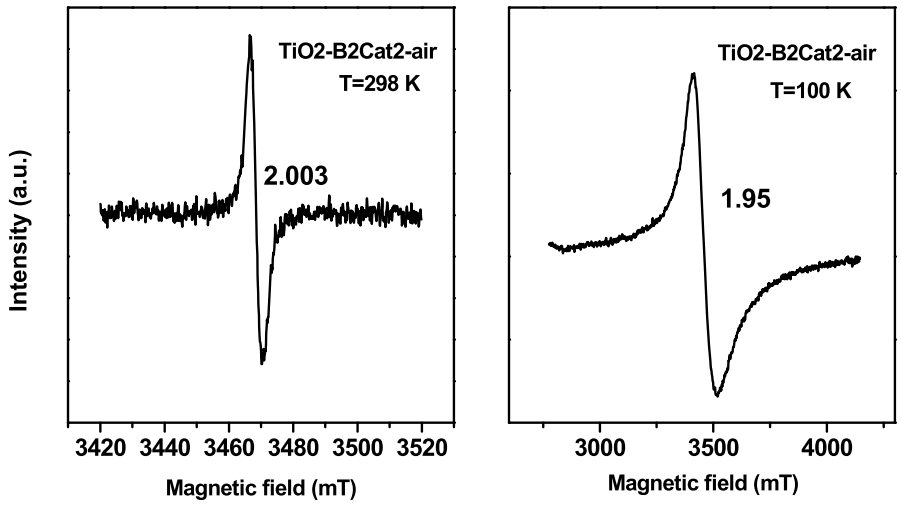

Figure S3. EPR signal of **B3**-TiO_2. Related to Figure 1.

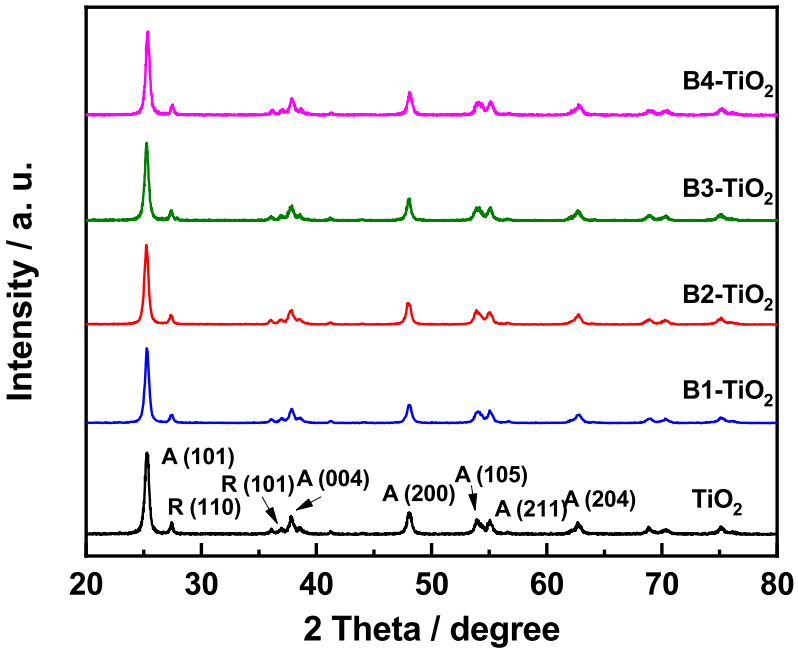

Figure S4. XRD pattern of boron compound adsorbed on TiO_2 by heat treatment at 80 °C and pristine TiO_2 (Degussa P25, A: anatase, R: rutile). Related to Figure 2.

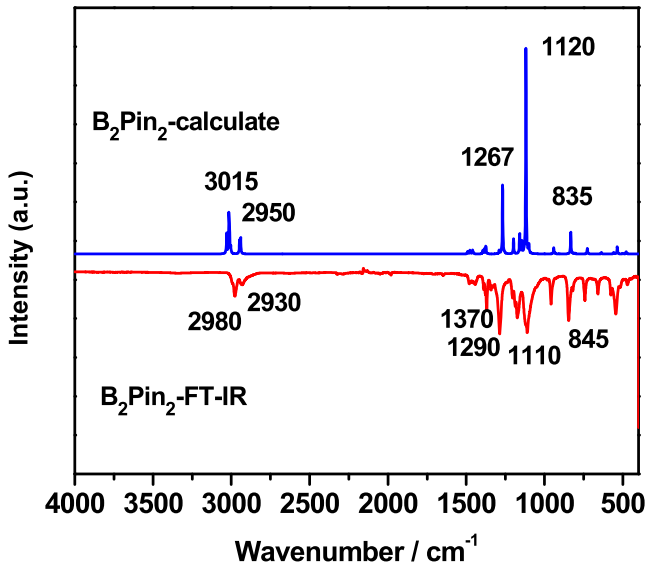

Figure S5. Calculated vibrational spectra of **B1** (B_2Pin_2, blue line) based on G09 package and experimental FT-IR transmission spectra (red line) (The frequency were corrected by a factor of 0.9614, at 6-31G* level). Related to Figure 2.

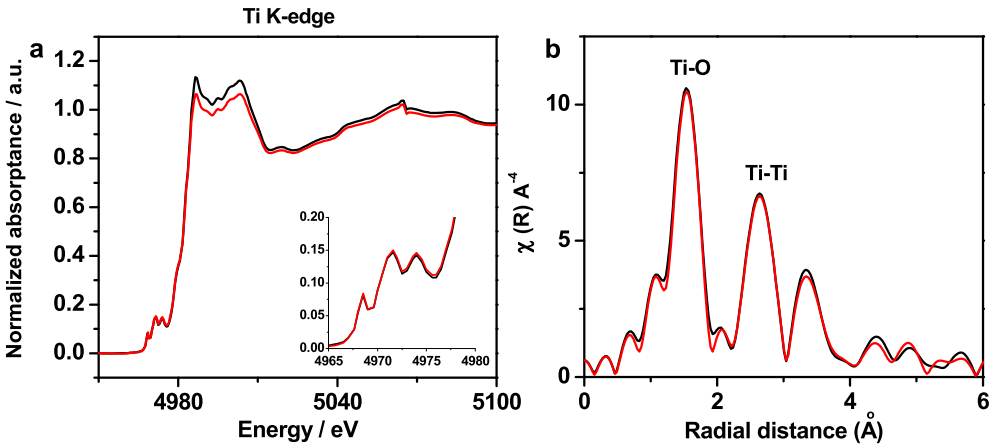

Figure S6. (A) Ti K edge line of **B3**-TiO_2 and pristine TiO_2. (B) Extend XAFS spectra of **B3**-TiO_2 and pristine TiO_2. Related to Figure 2.

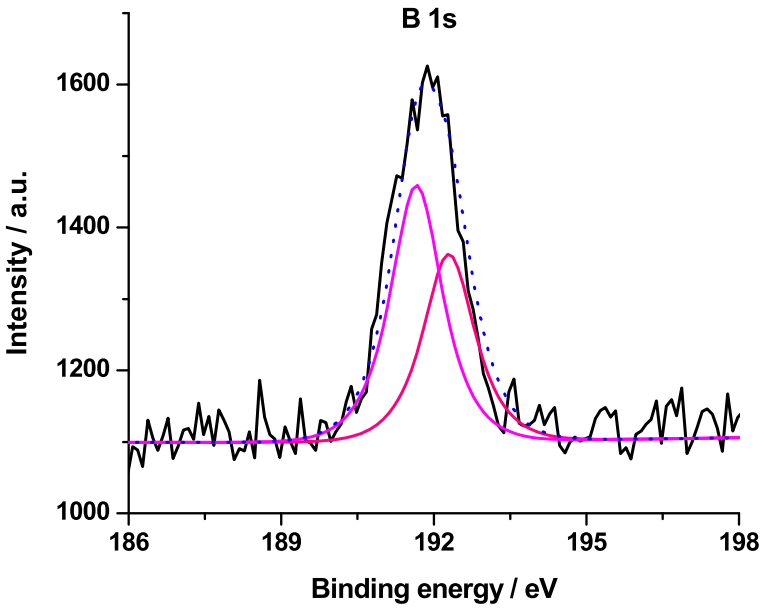

Figure S7. B 1s XPS spectra of **B1**-TiO_2 and simulate multiple peak fitting curve. Related to Figure 2.

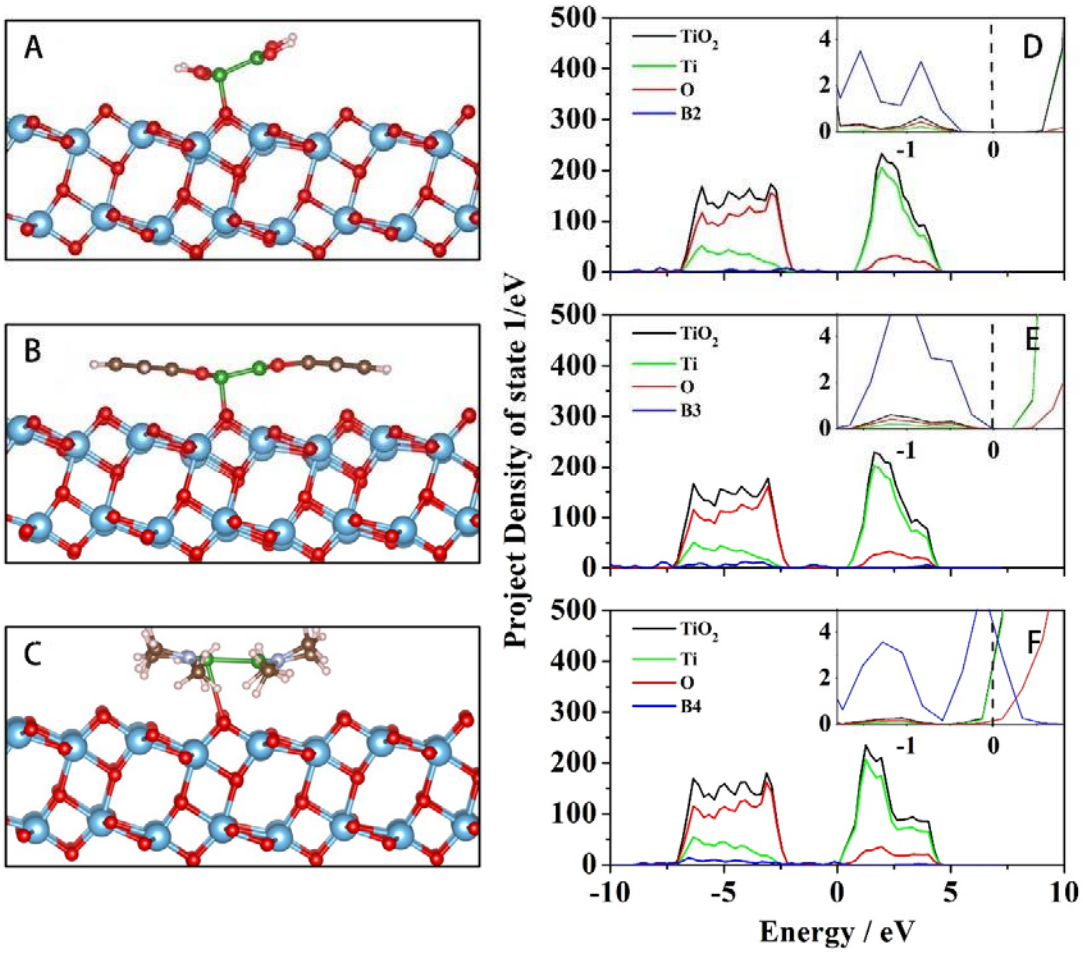

Figure S8. The optimized geometry structures of (A) **B2** $B_2(OH)_4$, (B) **B3** B_2Cat_2 and (C) **B4** $B_2(NMe_2)_4$ adsorbed TiO_2 {101} surface. Projected density of state (PDOS) plots of (D) **B2** $B_2(OH)_4$, (E) **B3** B_2cat_2 and (F) **B4** $B_2(NMe_2)_4$-adsorbed TiO_2 {101} surface. The dashed line stands for the Fermi level. Related to Figure 3.

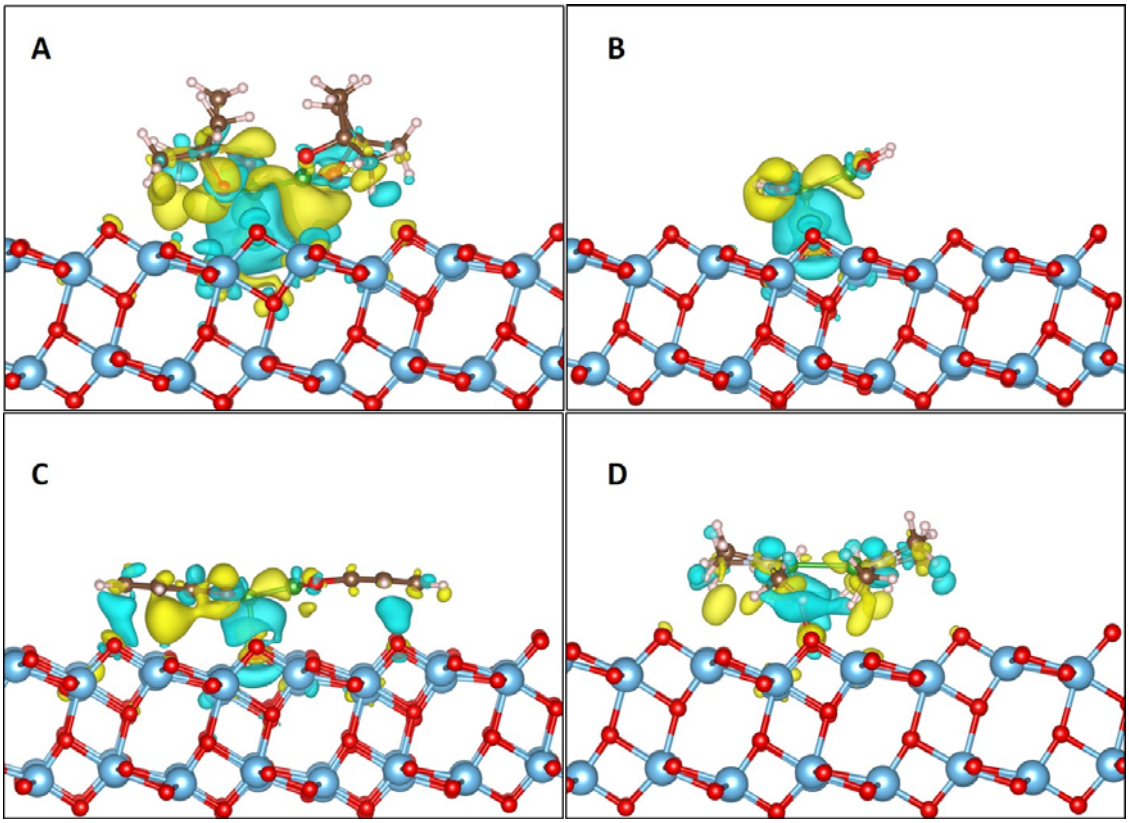

Figure S9. The optimized geometric structures and charge density difference plots of (A) **B1** B_2Pin_2 (B) **B2** $B_2(OH)_4$, (C) **B3** B_2Cat_2 and (D) **B4** $B_2(NMe_2)_4$ adsorbed TiO_2 {101} surface. The isosurface levels are set at 0.001 e $Å^{-3}$. The yellow and skyblue surfaces represent electron depletion and accumulation, respectively. Related to Figure 3.

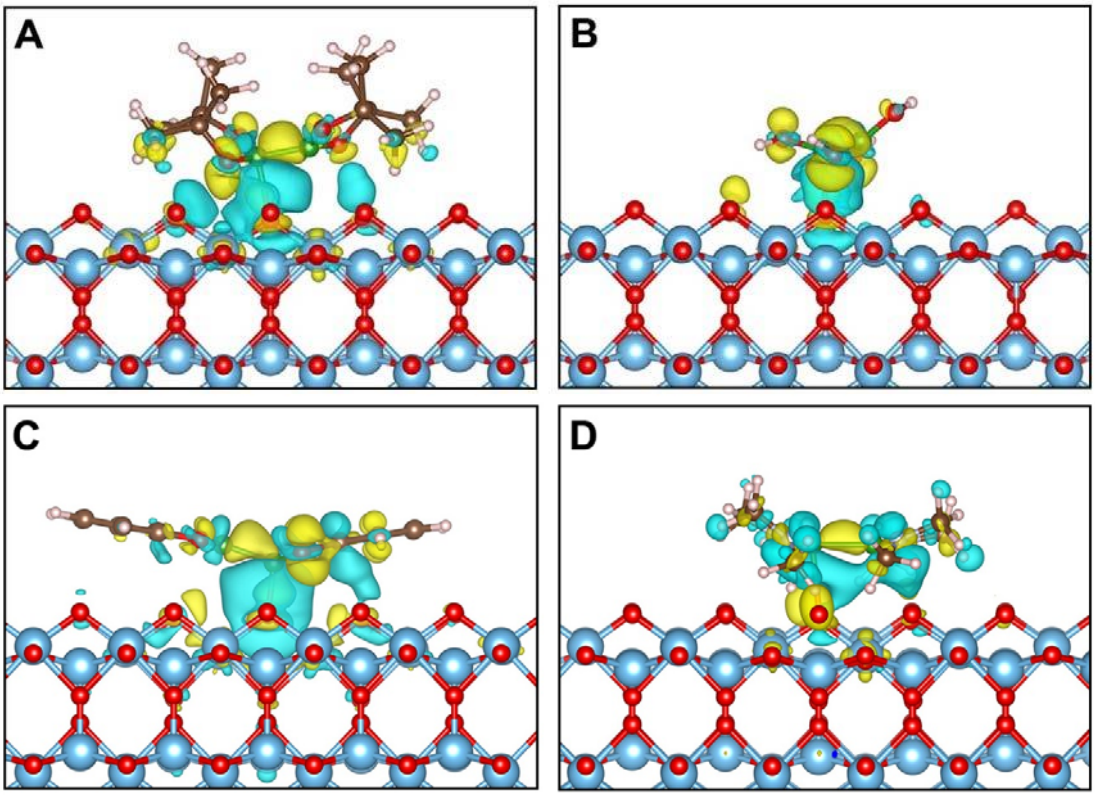

Figure S10. The optimized geometric structures and charge density difference plots of (A) **B1** B_2Pin_2 (B) **B2** $B_2(OH)_4$, (C) **B3** B_2Cat_2 and (D) **B4** $B_2(NMe_2)_4$ adsorbed on rutile TiO_2 {110} surface. The isosurface levels are set at 0.001 e $Å^{-3}$. Related to Figure 3.

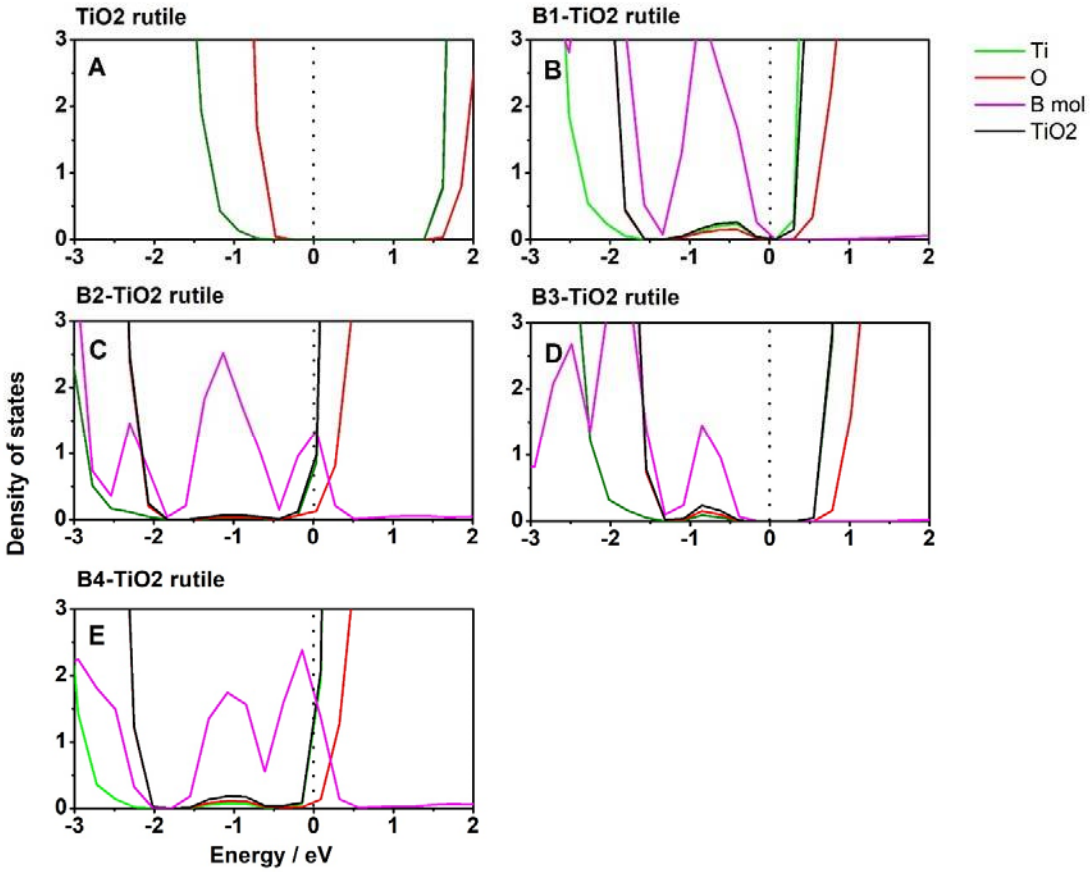

Figure S11. Projected density of state (PDOS) plots of (A) pristine TiO_2, (B) **B1** B_2Pin_2, (C) **B2** $B_2(OH)_4$, (D) **B3** B_2cat_2 and (E) **B4** $B_2(NMe_2)_4$-adsorbed rutile TiO_2 {110} surface. The dashed line stands for the Fermi level. Related to Figure 3.

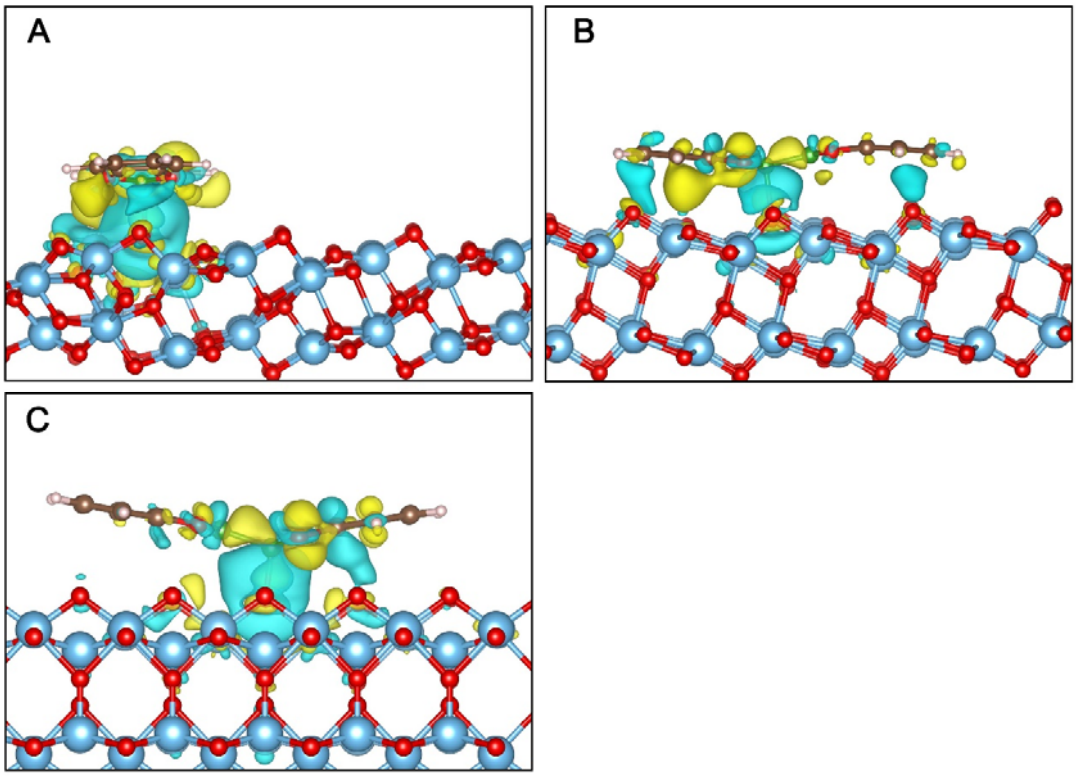

Figure S12. The isosurfaces of the electron density difference plots of B3 molecule adsorption on (A) the interface of anatase {112} (right) and rutile {101} (left) TiO_2 (phase ratio of anatase/rutile=8/3), (B) the surface of anatase {101}, (C) the surface of rutile {110}. The isosurfaces of the electron density difference plots are 0.001 e $Å^{-3}$. The yellow and light blue surfaces represent electron depletion and accumulation. The blue, red, yellow, green and pink spheres stand for the Ti, O, C, B and H atoms. Related to Figure 3.

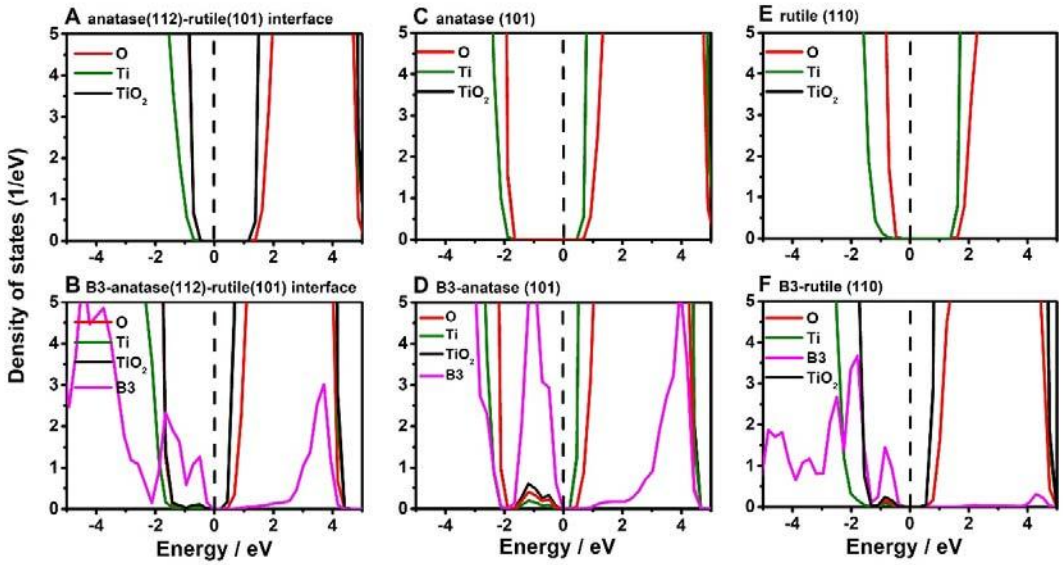

Figure S13. Projected density of states (PDOS) plots of (A) pristine B3 adsorption on the anatase{112}-rutile{101} interface, (B) B3 B_2cat_2-adsorbed anatase{112}-rutile{101} interface, (C) pristine anatase {101} surface, (D) B3 B_2cat_2-adsorbed anatase {101} surface, (E) pristine rutile {110} surface, (F) B3 B_2cat_2-adsorbed rutile {110} surface. The dashed lines stand for the Fermi level. Related to Figure 3.

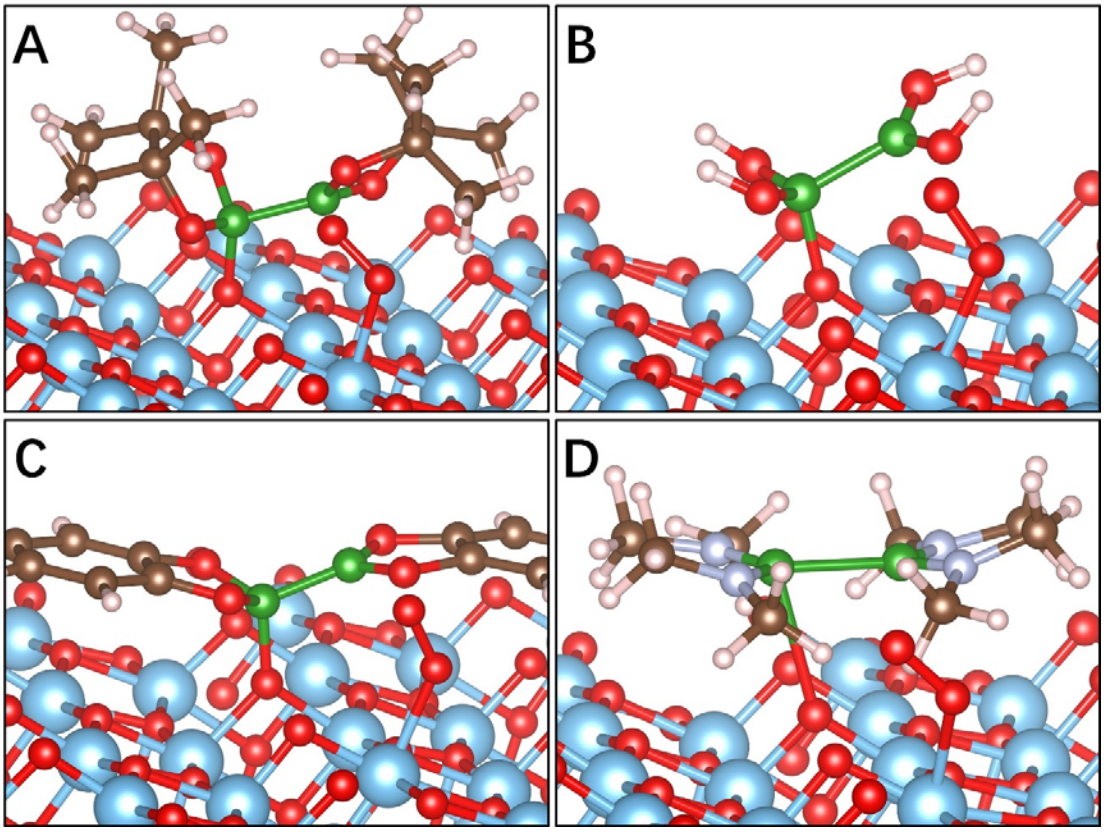

Figure S14. Optimized geometry structures of O_2 adsorption on the TiO_2 {101} plane of (A) **B1**-TiO_2, (B) **B2**-TiO_2, (C) **B3**-TiO_2, (D) **B4**-TiO_2 (adsorb to the Ti_{5c} site adjacent to the O_{2c} site with diboron compound adsorption). Related to Figure 3.

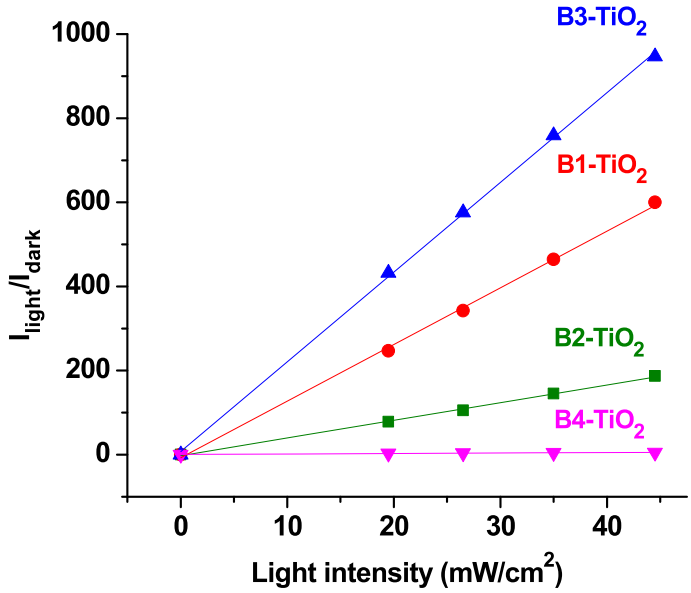

Figure S15. The simulated linear dynamic response SNR curve (signal to noise response). Related to Figure 4.

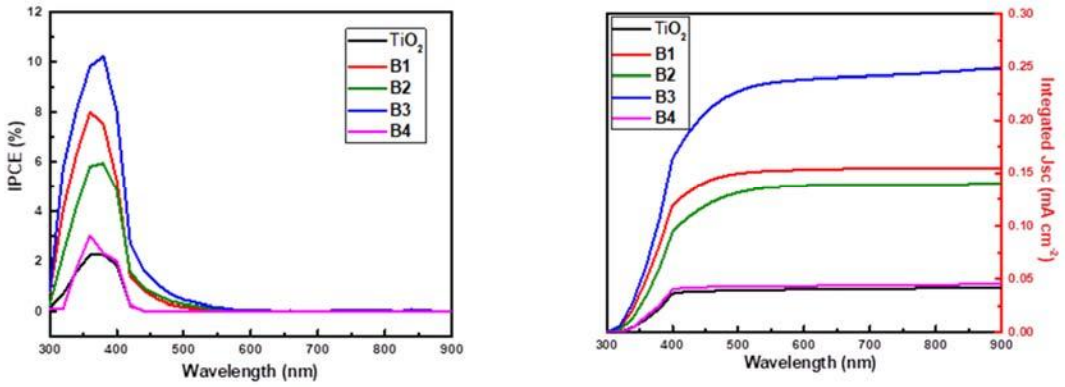

Figure S16. IPCE spectra of the photodetectors and the integration of the IPCE spectra for the photodetectors. Related to Figure 4.

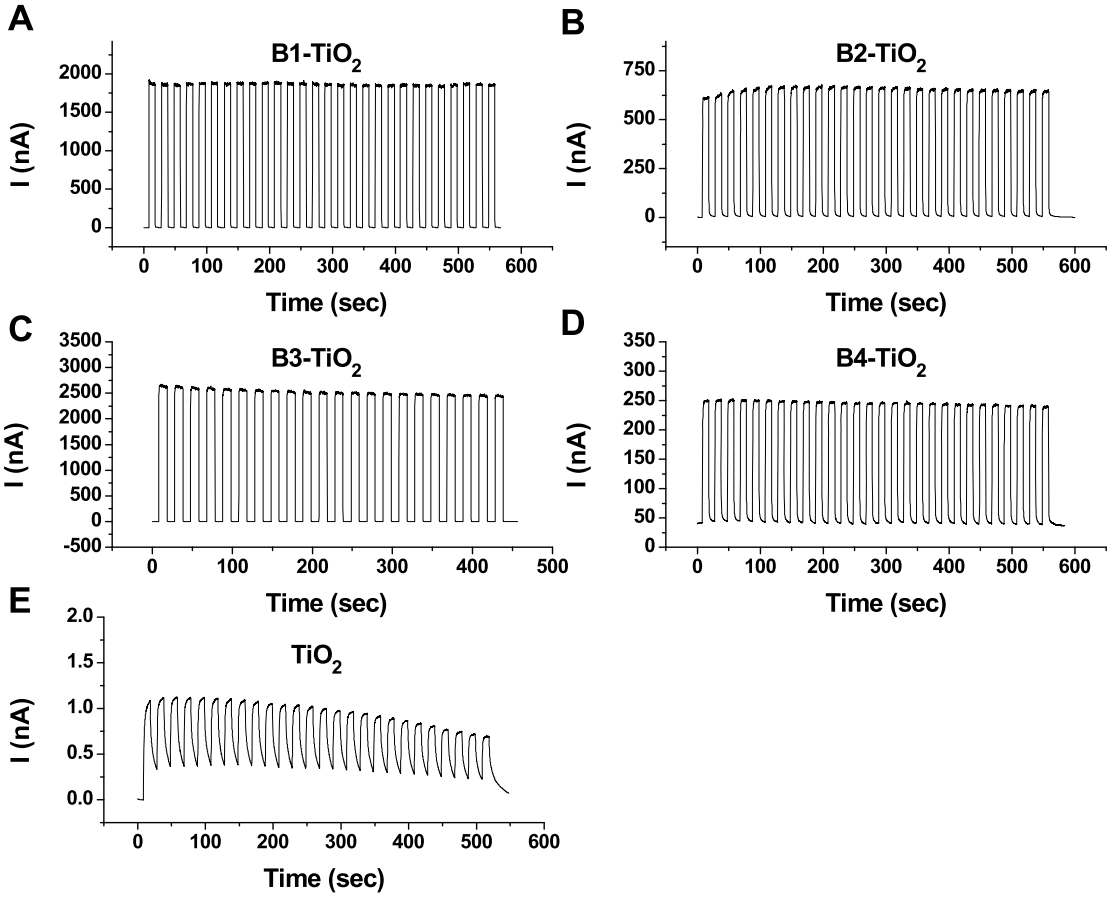

Figure S17. The transient photocurrent curve of the diboron compound devices and TiO_2 device alone with on off light switches ($\lambda > 400$ nm). Related to Figure 4.

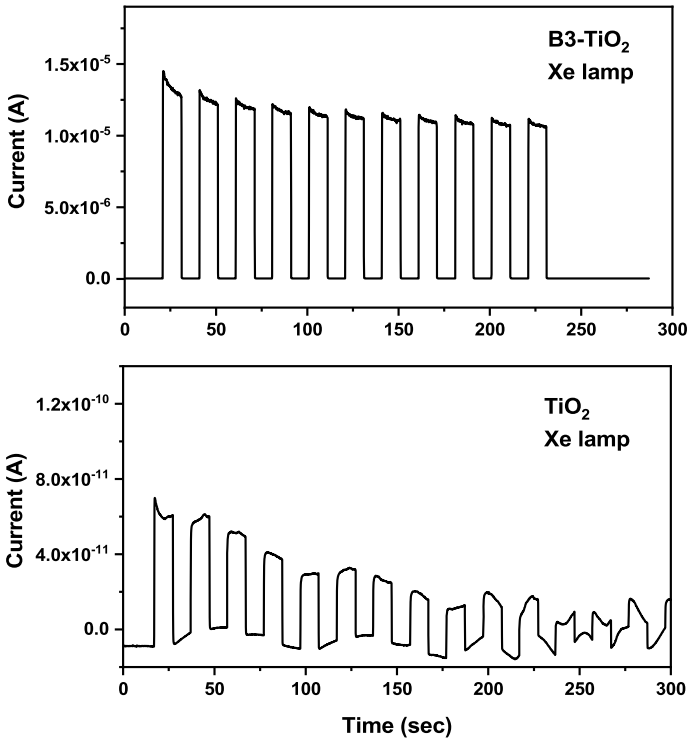

Figure S18. The comparation time dependent current curves for the **B3**-TiO_2 and TiO_2 detectors under light illumination with 10 s on/off switching intervals. (no cut off filter). Related to Figure 4.

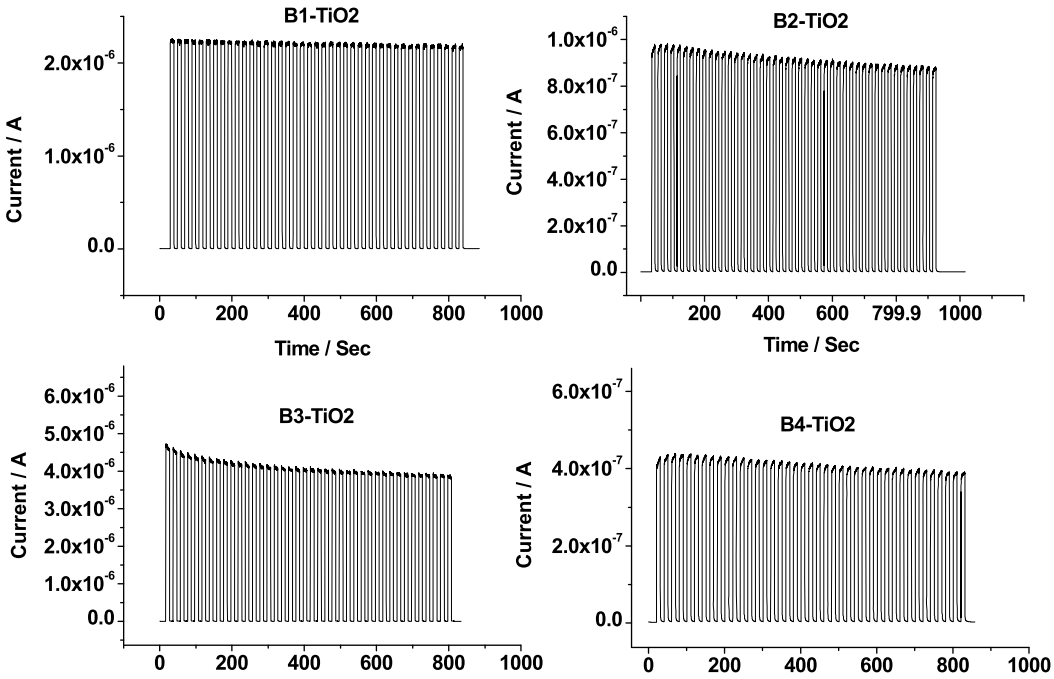

Figure S19. The transient photocurrent curve of the diboron compound device alone with on off light switches stored in the air atmosphere for 6 months (light source: 300 W Xe lamp with a 400 nm cut filter). Related to Figure 4.

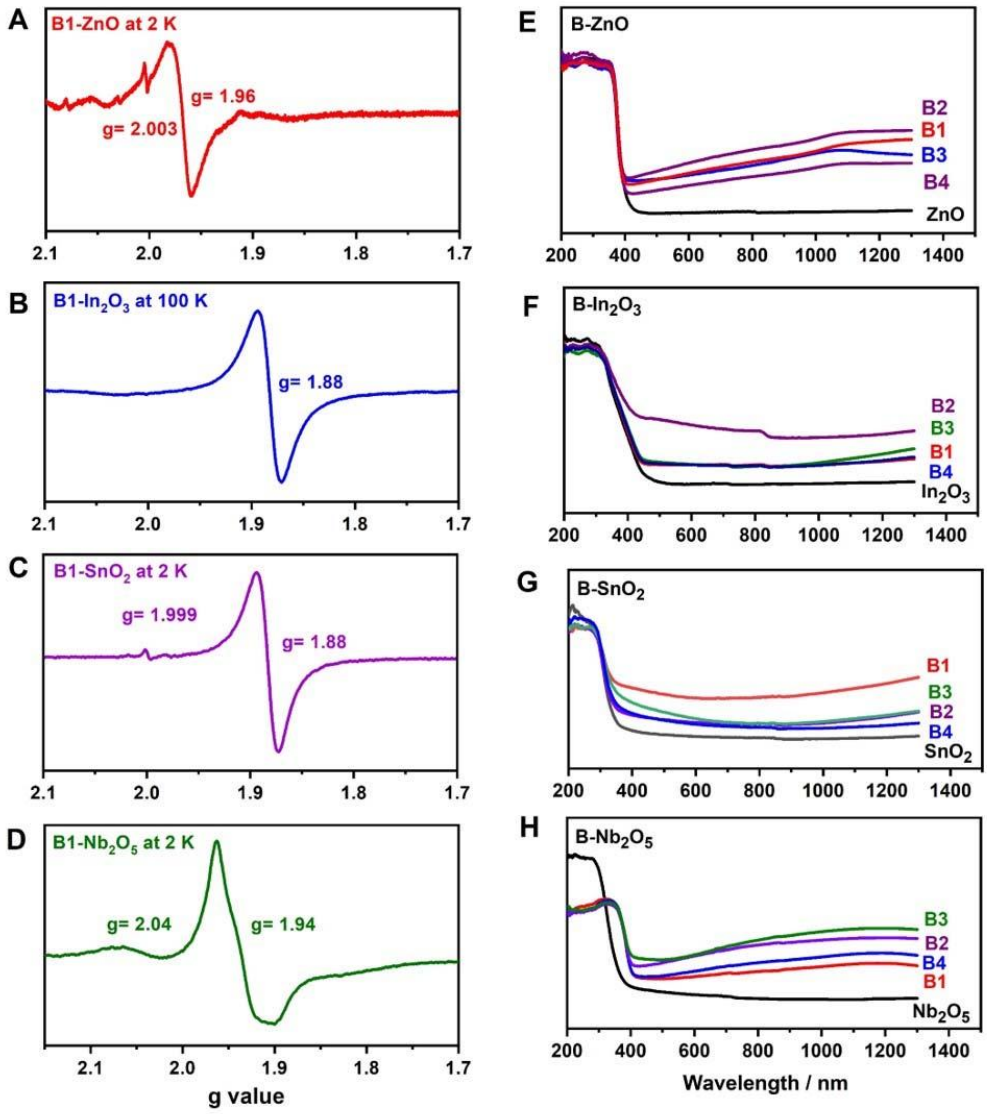

Figure S20. (A-D) EPR spectra of **B1**-metal oxides at various temperatures. (E-H) UV-Vis spectra of **B**-metal oxides. In these preliminary studies, by adopting a same adsorption operation to other common semiconductor oxides, such as ZnO, In_2O_3, SnO_2 and Nb_2O_5, similar phenomena were observed. EPR spectra demonstrated the appearance of reduced metal species, such as Zn^{+}, In^{2+}, Sn^{3+} and Nb^{4+}. Additionally, the UV-Vis of these modified materials were also collected. These diboron-modified metal oxides samples were found to absorb visible light with higher intensity in the NIR region. Related to Figure 4.

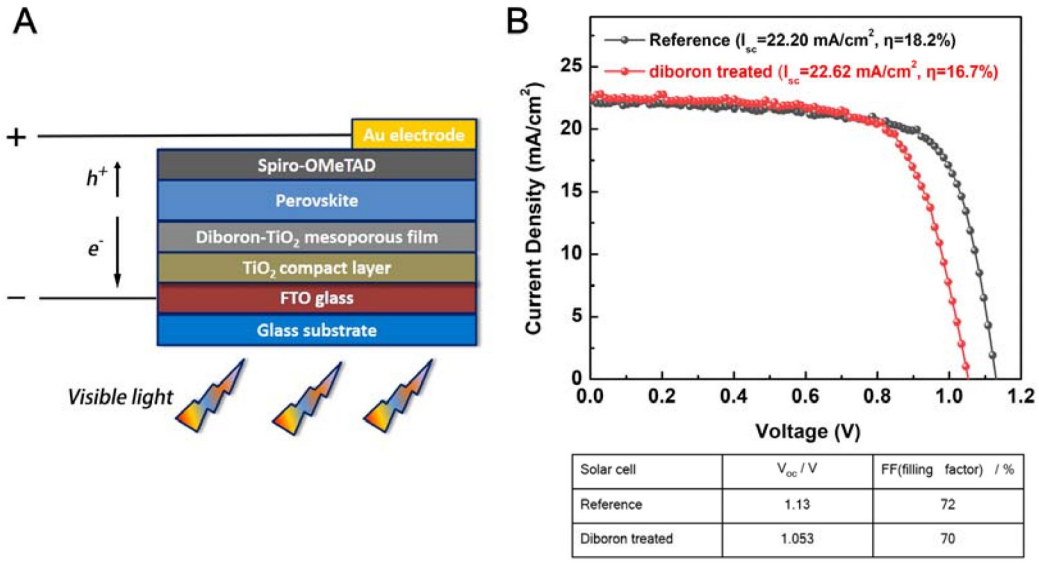

Solar cell	V_{oc} / V	FF(filling factor) / %
Reference	1.13	72
Diboron treated	1.053	70

Figure S21. (A) Schematic of the FTO/TiO_2/Perovskite/Spiro-OMeTAD/Au solar cell (B) Current density-voltage curves (J-V) of the diboron modified perovskite solar cell. Related to Figure 4.

Table S1. The adsorption energy of oxygen molecule to the diboron molecule pre-absorption TiO_2 {101} plane. Related to Figure 3.

	E(TiO_2-B)	E(O_2)	E(TiO_2-B-O_2)	E_{ad}
B1- TiO_2	-2063.56119598	-9.44011081	-2071.61712553	1.38418126
B2- TiO_2	-1883.20183442	-9.44011081	-1891.54740527	1.09453996
B3- TiO_2	-2002.25704951	-9.44011081	-2011.19765769	0.49950263
B4- TiO_2	-2028.25727155	-9.44011081	-2036.34654405	1.35083831

The adsorption energy of oxygen molecule to the diboron molecule pre-absorption TiO_2 {101} plane was calculated:

$$E_{ad} = E(TiO_2\text{-}B\text{-}O_2) - E(TiO_2\text{-}B) - E(O_2)$$

Table S2. The parameter of the photodetector devices. Related to Figure 4.

Photodetector	R (μA/W)	D (10^{12} Jones)	I_{light}/I_{dark}	SNR
TiO_2	0.18	27.7	3.06	2.05
B4-TiO_2	35.4	3.2	5.39	4.39
B2-TiO_2	151	9.3	214	213
B1-TiO_2	406	10.0	726	725
B3-TiO_2	814	8.9	778	777

The illumination power was calculated as P_{ill}= 44.5 mW/cm^2 × 0.0863 cm^2 = 3.84 mW.

The detail of the origin of the photocurrent

1. The responsivity R is calculated according to the equation:

$$R=(I_{light}-I_{dark})/P_{ill}$$

P_{ill} is definite as the illumination power on the photo harvest area of the device.

2. The light-detection ability of the photodetector can be evaluated by D:

$$D=R \times (S/2qI_{dark})^{1/2}$$

3. The signal-to-noise ratio (SNR) can be defined as:

$$SNR=(I_{light}-I_{dark})/I_{dark}$$

We get the amount of the diboron compounds by detection of B element concentration using ICP method (ICP-MS, iCAP Q, Thermo, Waltham, USA). We modified the mesoporous TiO_2 layer with diboron molecules as depicted in the experimental part. The mesoporous TiO_2 layer were then removed from the FTO glass and this sample was subject to ICP measurement. The results are given below.

Table S3. Amount of the diboron compounds on FTO glass. Related to Figure 4.

	c (B) μg/L (original data, amount of 4 FTO)	Diboron compound molecule weight	Diboron compound mass per FTO (μg)	Diboron compound molar per FTO (μmol)
B1- TiO_2	794.8	253.94	22.9354	0.090318
B2- TiO_2	1027	89.65	10.46256	0.116705
B3- TiO_2	1037.6	237.81	28.03996	0.117909
B4- TiO_2	775	197.92	17.43045	0.088068

Reference:

Perdew, J.P., Burke, K., and Ernzerhof, M. (1996). Generalized Gradient Approximation Made Simple. Phys Rev Lett *77*, 3865-3868.
Perdew, J.P., and Wang, Y. (1992). Accurate and simple analytic representation of the electron-gas correlation energy. Phys Rev B *45*, 13244-13249.
Zhao, W.-N., Zhu, S.-C., Li, Y.-F., and Liu, Z.-P. (2015). Three-phase junction for modulating electron–hole migration in anatase–rutile photocatalysts. Chemical Science *6*, 3483-3494.